

# Density Functional Theory: The Car-Parrinello Method

Nickolas Theodoulou  
Supervisor: Prof. Keith Refson

March 26, 2019

## Abstract

Density functional theory makes it possible for the ground state properties of a system of electrons in an external field to be determined by the electron density distribution alone. The Kohn-Sham equations will be derived and the approximations used will be discussed. This review will highlight various applications of the Car-Parrinello method for material science, condensed matter physics and medicine. There will be a particular focus on reviewing recent papers that apply the Car-Parrinello method to the liquid structure of water.

## Contents

<b>I.</b>	<b>Introduction</b>	<b>3</b>
	A. A Brief Summary of Density Functional Theory . . . . .	3
	B. Outline . . . . .	4
<b>II.</b>	<b>Theoretical Background: Deriving the Kohn-Sham Equations</b>	<b>4</b>
	A. Finding the Many-Body Schrödinger equation in Hartree atomic units . . . . .	4
	B. Clamped Nuclei Approximation . . . . .	5
	C. Independent Electron Approximation . . . . .	6
	D. Considering the Pauli exclusion principle . . . . .	6
	E. Mean-Field Approximation . . . . .	6
	F. Hartree-Fock equations . . . . .	7
	G. Hohenberg-Kohn theorem . . . . .	7
	H. The Exchange and Correction Energy . . . . .	8
	I. The Kohn-Sham equations . . . . .	9
	J. Self Consistency . . . . .	9
<b>III.</b>	<b>Methods used to solve the Kohn-Sham equations</b>	<b>9</b>
	A. Basis Sets: Gaussians and Slater Functions . . . . .	9
	B. Basis Sets: Plane Waves . . . . .	10
	C. Pseudopotentials . . . . .	10
	D. Numerical solution of the Kohn-Sham equations . . . . .	11
<b>IV.</b>	<b>Car-Parrinello Molecular Dynamics</b>	<b>11</b>
	A. The Car-Parrinello Lagrangian and equations of motion . . . . .	11
	B. Why the Car-Parrinello method works . . . . .	13
<b>V.</b>	<b>Application of Density-Functional Theory</b>	<b>14</b>
	A. Semiconductor Photocatalysis . . . . .	14
	B. Simulations of Methylammonium Lead Iodide Perovskite Degradation by Water . . . . .	15
	C. Biological Systems: Prions . . . . .	15
	D. Biological Systems: HIV-1 Protease Cleavage Site . . . . .	15
<b>VI.</b>	<b>The Structure of Water</b>	<b>16</b>
	A. Computational papers . . . . .	17
	B. Larger simulations . . . . .	19
	C. The diffusion of water . . . . .	19
	D. Recent Papers on Hybrid Functionals . . . . .	21

<b>VII. Accounting for the Van Der Waals Forces</b>	<b>21</b>
A. Examples of the limitation of XC functionals in systems involving dispersion . . . . .	22
B. Common DFT based dispersion methods . . . . .	22
B.1 Binding with incorrect asymptotics . . . . .	23
B.2 Simple $C_6$ corrections . . . . .	23
<b>VIII. Summary and Conclusion</b>	<b>24</b>
A. Summary . . . . .	24
B. Conclusion . . . . .	25

# I. Introduction

## A. A Brief Summary of Density Functional Theory

Density functional theory (DFT) is a computational method used to study solids, nanostructures, molecules, surfaces and interfaces by directly solving approximate versions of the Schrödinger equation. The foundation of the theoretical framework of DFT was established with the paper published by Hohenberg and Kohn in 1964 titled “Inhomogeneous electron gas” [1].

To summarize, the paper describes the ground state of an interacting electron gas in an external potential  $v(\mathbf{r})$ . It proves that there exists a universal functional of the electron density distribution,  $F[n(\mathbf{r})]$ , independent of  $v(\mathbf{r})$  such that the total energy given by

$$E = \int v(\mathbf{r})n(\mathbf{r})d\mathbf{r} + F[n(\mathbf{r})], \quad (1)$$

has the ground state energy associated with  $v(\mathbf{r})$  as its minimum value. This model of a gas of electrons can be applied to develop reliable *ab initio* models of materials. For a system of electrons in the presence of ions located at  $R_1$ , accurate calculations of the entire energy surface,  $E(R_1)$ , are only possible for very few atoms. This is because  $E(R_1)$  has a vast number of minima and maxima. The lowest energy corresponds to the ground state structure and paths between minima are fundamental to the studies of chemical reactions. DFT makes it possible to calculate  $E(R_1)$  without using experimental input.

Until 1985, there were a total of just 77 publications in the field of DFT as up until that time, density functional calculations in chemistry and condensed matter did not find universal acceptance [2]. An important paper was written in 1985 by Car and Parrinello in which density functional calculations are combined with Molecular dynamics [3]. This introduced Car-Parrinello molecular dynamics (CPMD) and will be the topic of Sec.IV.. The Car-Parrinello (CP) method is what allowed *ab initio* molecular dynamics (AIMD) simulations to be feasible for the first time. In this model, the potential surface energy is generated on the fly from the instantaneous ground state density of the electrons defined using DFT [4]. This simulation method that combines the classical molecular dynamics of nuclei with electronic structure theory is known as AIMD.

After the publication of Ref.[3], there was a dramatic increase in the number of publications on DFT topics which has continued to grow. This can be seen in Fig.1 . A reason for this growth is that there are several AIMD easy-to-use program packages that are currently available for academics making it possible to apply the method without the need to understand all the technical aspects of it. Some reasons as to why CPMD works effectively will be discussed in some detail in Sec.IV. B.. The original CP method uses Kohn-Sham density functional theory within the pseudopotential plane wave framework [5].

AIMD can also be used in a large variety of systems such as wet DNA [6] as well as amorphous silicon [7]. Various other applications in a broad spectrum of fields is the topic of SecV.. Due to such a wide application of the method, there is a relatively large demand for academic software. Because of this, the software packages are constantly being improved upon thus improving the overall quality of the research. This is another reason for large growth of the field.

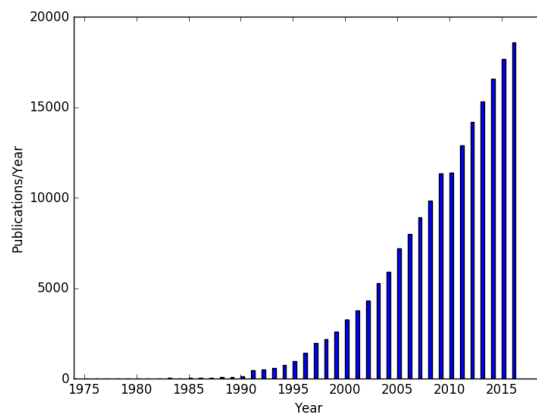


Fig. 1: Number of publications per year (1975-2016) on topics “Density Functional Theory” or “DFT” using data gathered from Web of Knowledge. Figure adapted from Ref.[2].

## B. Outline

The purpose of this review is to first introduce the reader to DFT by first discussing the background which is essential to understand recently published papers. Various applications of DFT in medicine and material science will then be highlighted to show the wide scope of the field. The application of DFT on the structure of liquid water will then be reviewed in depth. Conclusions will be drawn as to what may cause some limitations of DFT when applied to the structure of water. A more in depth overview of each section and some motivations as to why they are included will now be discussed.

In Sec.II., the Kohn-Sham (KS) equations are derived by first starting with the many-body Schrödinger equation. These are the equations that are solved computationally for systems using CPMD software packages. Various approximations are also discussed in the Section so that the reader is familiar with what assumptions have been made to arrive at the KS equation. In particular, Sec.II.H. introduces what is known as the Exchange and correction potential, something that is constantly referred to throughout the review as it is currently an important field of research.

Sec.III. briefly covers the most important methods that are used in material modeling. This includes the plane wave basis set that can be used to define the Hartree potential introduced in Sec.II. which is essential in having some idea as to how the KS equations are solved computationally discussed in Sec.III.D.. In Sec.IV., the Car–Parinello equations of motions are highlighted. These are the equations of motion that are solved using the methods mentioned in Sec.III. such as plane waves and pseudopotentials in CPMD to model systems.

The rest of this review article will focus on research in DFT. Sec.V. will highlight examples of material modelling using DFT such as applications in medicine and material science. Sec.VI. will focus on the application of DFT to the structure of water and also discuss recent papers in the field. Various inconsistencies such as the diffusion coefficient being incorrect will be discussed. Sec.VII. will then discuss recent papers that introduce the Van Der Waals force into the simulation of liquid water. This gives a better description of the system and also improves upon some of the inconsistencies previously mentioned. In Sec.VIII. the review will be summarised and various conclusions as to where the inconsistencies of the CP method arise will be drawn.

## II. Theoretical Background: Deriving the Kohn-Sham Equations

In this section, the KS equations are derived starting with the many-body Schrödinger equation. The main purpose of this section is to highlight the approximations and assumptions that are used to arrive at the KS equations.

### A. Finding the Many-Body Schrödinger equation in Hartree atomic units

The many-body Schrödinger equation is given by

$$\left[ -\sum_i \frac{\hbar^2}{2m_e} \nabla_i^2 - \sum_I \frac{\hbar^2}{2M_I} \nabla_I^2 + \frac{1}{2} \sum_{i \neq j} \frac{e^2}{4\pi\epsilon_0} \frac{1}{|\mathbf{r}_i - \mathbf{r}_j|} + \frac{1}{2} \sum_{I \neq J} \frac{e^2}{4\pi\epsilon_0} \frac{Z_I Z_J}{|\mathbf{R}_I - \mathbf{R}_J|} - \sum_{i,I} \frac{e^2}{4\pi\epsilon_0} \frac{Z_I}{|\mathbf{r}_i - \mathbf{R}_I|} \right] \Psi = E_{\text{tot}} \Psi, \quad (2)$$

where the symbols have their usual meaning. The first two terms represent the kinetic energy of the electrons and nuclei respectively, the third term the Coulomb repulsion between electron pairs, the fourth term Coulomb repulsion between pairs of nuclei and the final term the Coulomb attraction between electrons and nuclei. The summation indices  $i, j$  and  $I, J$  run from 1 to  $N$  and 1 to  $M$  respectively where  $N$  is the number of electrons and  $M$  is the number of nuclei. A derivation of this can be found in many textbooks such as “Materials modelling using Density Functional Theory” by Feliciano Giustino [8].

In theory, the many-body Schrödinger Eq.(2) can be solved and the ground state of the system can be determined making it possible to calculate many equilibrium properties of the materials. Some of which include: phase diagrams, elastic properties and thermal properties. However, the solution for systems with more than a few particles is very difficult and in most cases, practically impossible and therefore the many-body Schrödinger equation must be simplified.

To further simplify Eq.(2), it is important to note that the fundamental constants  $\hbar, m_e, m_p, e, \epsilon_0$  do not depend on the particular material under construction. As there are no empirical parameters, it is known as a “first-principles approach”. The average Coulomb energy of an electron–proton pair in the Hydrogen atom is given by

$$E_{\text{Ha}} = \frac{e^2}{4\pi\epsilon_0 a_0} \quad (3)$$

where “Ha” denotes “Hartree” and  $a_0 \simeq 0.529 \text{ \AA}$ . This approximation gives a sense of the order of magnitude of the energies involved. As  $E_{\text{Ha}}$  gives the Coulomb energy for a pair of two protons or a pair of two electrons

at the same distance, it is suitable to assume that the potential term in Eq.(2) is also of the order  $E_{\text{Ha}}$ . A semi-classical argument introduced by Bohr in 1913 to quantise the H atom can then be used [9]. In this model, the electron's trajectories are given by

$$m_e v a_0 = \hbar, \quad (4)$$

where  $v$  is the electron velocity. By equating the centrifugal force and the nuclear attraction, the following result is obtained:

$$m_e \frac{v^2}{a_0} = \frac{e^2}{4\pi\epsilon_0 a_0^2}. \quad (5)$$

By combining Eq.(3-5), the following results are obtained:

$$\frac{e^2}{4\pi\epsilon_0 a_0} = \frac{\hbar^2}{m_e a_0^2} \quad \text{and} \quad \frac{1}{2} m_e v^2 = \frac{1}{2} E_{\text{Ha}}. \quad (6)$$

This suggests that the kinetic energy is also of the order of  $E_{\text{Ha}}$  making it possible to simplify Eq.(2) by dividing it by  $E_{\text{Ha}}$ . Using Hartree atomic units where  $e = \hbar = c = 1$ , the many-body Schrödinger equation can be expressed more elegantly as

$$\left[ -\sum_i \frac{\nabla_i^2}{2} - \sum_I \frac{\nabla_I^2}{2M_I} - \sum_{i,I} \frac{Z_I}{|\mathbf{r}_i - \mathbf{R}_I|} + \frac{1}{2} \sum_{i \neq j} \frac{1}{|\mathbf{r}_i - \mathbf{r}_j|} + \frac{1}{2} \sum_{I \neq J} \frac{Z_I Z_J}{|\mathbf{R}_I - \mathbf{R}_J|} \right] \Psi = E_{\text{tot}} \Psi. \quad (7)$$

In first-principles materials modeling, this is the most commonly used form of the Many-Body Schrödinger Equation.

## B. Clamped Nuclei Approximation

The Many-Body Schrödinger equation, Eq.(7), is a very general equation meaning that solving it computationally would be extremely inefficient. One method to simplify the equation would be to use the clamped nuclei approximation. This is possible due to the Born–Oppenheimer approximation which assumes that the motion of atomic nuclei and electrons in a molecule can be separated such that the total wave-function reads

$$\Psi_{\text{total}} = \Psi_{\text{electronic}} + \Psi_{\text{nuclear}}. \quad (8)$$

In the case of solids, nuclei typically remain at or near certain positions. Due to this, a good starting point would be to assume that the nuclei are clamped in known positions. This condition can be interpreted as an ordered crystalline lattice, a molecule structure or an amorphous structure where only the electrons can move. To apply this condition,  $M_I = \infty$  is set in Eq.(7) such that the kinetic energy of the nuclei is ignored and the Coulomb repulsion between the nuclei become a constant. The constant is brought to the right hand side by defining

$$E = E_{\text{tot}} - \frac{1}{2} \sum_{I \neq J} \frac{Z_I Z_J}{|\mathbf{R}_I - \mathbf{R}_J|}. \quad (9)$$

The nuclear coordinates,  $\mathbf{R}_I$ , can be treated as external parameters so the wave function can be considered as a function only of the electron coordinates thus giving the equation:

$$\left[ -\sum_i \frac{\nabla_i^2}{2} + \sum_i V_n(\mathbf{r}_i) + \frac{1}{2} \sum_{i \neq j} \frac{1}{|\mathbf{r}_i - \mathbf{r}_j|} \right] \Psi = E \Psi = \hat{H}(\mathbf{r}_1, \dots, \mathbf{r}_N) \Psi. \quad (10)$$

From this equation, it is useful to define the single-electron Hamiltonian as

$$\hat{H}_0(\mathbf{r}) = -\frac{\nabla^2}{2} + V_n(\mathbf{r}), \quad (11)$$

so that the many-electron Hamiltonian can be written as

$$\hat{H}(\mathbf{r}_1, \dots, \mathbf{r}_N) = \sum_i \hat{H}_0(\mathbf{r}_i) + \frac{1}{2} \sum_{i \neq j} \frac{1}{|\mathbf{r}_i - \mathbf{r}_j|}. \quad (12)$$

It is important to note however that the nuclei in a physical material are not immobile due to the uncertainty principle  $\Delta x \Delta p \geq \hbar$ .

### C. Independent Electron Approximation

The electrons can be treated as being independent by eliminating the term describing the Coulomb interaction between the electrons in the many-body Schrödinger equation giving the equation

$$\sum_i \hat{H}_0(\mathbf{r}_i) \Psi = E \Psi. \quad (13)$$

The solutions to this can be written as a product of wavefunctions such that

$$\Psi(\mathbf{r}_1, \mathbf{r}_2, \dots, \mathbf{r}_N) = \phi_1(\mathbf{r}_1) \dots \phi_N(\mathbf{r}_N). \quad (14)$$

The wave functions,  $\phi_i$  can be obtained as the solution of the single electron Schrödinger equations by

$$\hat{H}_0(\mathbf{r}) \phi_i(\mathbf{r}) = \epsilon_i \phi_i(\mathbf{r}), \quad (15)$$

where  $\epsilon_1$  is the smallest eigenvalue and  $\epsilon_1 < \epsilon_2 < \dots < \epsilon_N$ . It is important to note that ignoring the electron–electron interaction has a large effect on the system so a correction will be added in Sec.II.E..

### D. Considering the Pauli exclusion principle

It should be noted that Eq.(14) violates the Pauli exclusion principle which requires that  $\Psi(\mathbf{r}_2, \mathbf{r}_1) = -\Psi(\mathbf{r}_1, \mathbf{r}_2)$ . It is later accounted for in the exchange potential term,  $V_X$  in Sec.II.F.. In DFT, as the Pauli Exclusion principle is included by other means, the wave-function description of a state is not used. The wave-function that obeys the Pauli exclusion principle is written as

$$\Psi(\mathbf{r}_1, \mathbf{r}_2) = \frac{1}{\sqrt{2}} \begin{vmatrix} \phi_1(\mathbf{r}_1) & \phi_1(\mathbf{r}_2) \\ \phi_2(\mathbf{r}_1) & \phi_2(\mathbf{r}_2) \end{vmatrix}, \quad (16)$$

which is referred to as a Slater determinant [10]. This can be generalized to  $N$  fermions giving the equation

$$\Psi(\mathbf{r}_1, \dots, \mathbf{r}_N) = \frac{1}{\sqrt{N!}} \begin{bmatrix} \phi_1(\mathbf{r}_1) & \dots & \phi_1(\mathbf{r}_N) \\ \vdots & \ddots & \vdots \\ \phi_N(\mathbf{r}_1) & \dots & \phi_N(\mathbf{r}_N) \end{bmatrix}. \quad (17)$$

What is useful to draw from this wave-function description is that the electron charge density is obtained by adding up the probability of finding the electron in each occupied state  $i$  in Eq.(17) defined as

$$n(\mathbf{r}) = \sum_i |\phi_i(\mathbf{r})|^2. \quad (18)$$

This is an important concept in the Kohn-Sham model. It is also important to note that

$$\int d\mathbf{r} \phi_i^*(\mathbf{r}) \phi_j(\mathbf{r}) = \delta_{ij}, \quad (19)$$

is a direct consequence of Eq.(15) if the energy,  $E$ , of the system is minimized where  $\delta_{ij}$  is the Kronecker delta [11].

### E. Mean-Field Approximation

As mentioned before, not including the Coulomb interaction between the electrons has a large effect on the system so an approximation of the Coulomb repulsion needs to be used. One way of doing this is by considering the electrostatic potential  $\phi(\mathbf{r})$  through Poisson's equation given by

$$\nabla^2 \phi(\mathbf{r}) = 4\pi n(\mathbf{r}). \quad (20)$$

In Hartree units, the Hartree potential energy is given by  $V_H(\mathbf{r}) = -\phi(\mathbf{r})$ . By definition this potential also satisfies Poisson's equation:

$$\nabla^2 V_H(\mathbf{r}) = -4\pi n(\mathbf{r}), \quad (21)$$

which has the solution

$$V_H(\mathbf{r}) = \int d\mathbf{r}' \frac{n(\mathbf{r}')}{|\mathbf{r} - \mathbf{r}'|}. \quad (22)$$

So far, we have the Hartree equations:

$$\left[ -\frac{\nabla^2}{2} + V_n(\mathbf{r}) + V_H(\mathbf{r}) \right] \phi_i(\mathbf{r}) = \epsilon_i \phi_i(\mathbf{r}), \quad (23)$$

$$\nabla^2 V_H(\mathbf{r}) = -4\pi n(\mathbf{r}), \quad (24)$$

$$n(\mathbf{r}) = \sum_i |\phi_i(\mathbf{r})|^2, \quad (25)$$

which is a large simplification to the many-body Schrödinger equation. A limitation of this however, is that the solutions of  $\phi_i$  are coupled through the electron density  $n(\mathbf{r})$  therefore the equations need to be solved using iterative numerical methods. As Eq.(23-25) must be solved simultaneously, the approach is known as a self-consistent field method which was introduced by Hartree [12].

## F. Hartree-Fock equations

The Hartree-Fock equations can be obtained by first assuming that an anti-symmetric Slater determinant given in Eq.(17) is the solution to Eq.(10). Then, if the energy,  $E$ , is minimized with respect to variations of the functions  $\phi_i(\mathbf{r})$  such that

$$\frac{\delta E}{\delta \phi_i^*} = 0, \quad (26)$$

and the functions are orthonormal via Eq.(19) the Hartree-Fock equations can be obtained. They are defined as

$$\left[ -\frac{\nabla^2}{2} + V_n(\mathbf{r}) + V_H(\mathbf{r}) \right] \phi_i(\mathbf{r}) + \int d\mathbf{r}' V_X(\mathbf{r}, \mathbf{r}') \phi_i(\mathbf{r}') = \epsilon_i \phi_i(\mathbf{r}), \quad (27)$$

as well as Eq.(24) and Eq.(25). By comparing Eq.(27) with Eq.(23-25) we can see that there is an additional potential defined as

$$V_X(\mathbf{r}, \mathbf{r}') = - \sum \frac{\phi_j^*(\mathbf{r}') \phi_j(\mathbf{r})}{|\mathbf{r} - \mathbf{r}'|}, \quad (28)$$

where the sum is over the occupied single-particle states [13]. The potential  $V_X(\mathbf{r}, \mathbf{r}')$  is non-local as Eq.(28) includes an integration over an additional variable  $\mathbf{r}'$  which complicates the solution of the Hartree-Fock equations. The function  $V_X$  arises from the Pauli exclusion principle as it is the potential term that prevents two electrons occupying the same quantum state.

As the potential  $V_X$  is summed over the additional variable  $\mathbf{r}'$ , it will be replaced with a simplified local exchange potential  $V_x$  which depends on only one spacial coordinate. Currently the Coulomb repulsion includes the three terms  $V_n + V_H + V_x$  in the single particle equations. There is one element that hasn't been accounted for which is known as the *correlation* between the electrons which can be defined as  $V_c$ . By putting together the approximations, we arrive at the equation

$$\left[ -\frac{\nabla^2}{2} + V_n(\mathbf{r}) + V_H(\mathbf{r}) + V_x(\mathbf{r}) + V_c(\mathbf{r}) \right] \phi_i(\mathbf{r}) = \epsilon_i \phi_i(\mathbf{r}). \quad (29)$$

The potentials  $V_x(\mathbf{r})$  and  $V_c(\mathbf{r})$  however do not have an exact form and have not been determined. Useful approximations have been made for the potential terms  $V_x(\mathbf{r})$  and  $V_c(\mathbf{r})$  which are central to first principles materials modelling will be discussed in Sec.II.H.. Equations such as Eq.(29) are known as Kohn-Sham equations and were first introduced by Kohn and Sham in 1965 in a paper titled "Self-Consistent Equations Including Exchange and Correlation Effects" [14].

## G. Hohenberg-Kohn theorem

The core concept of DFT is that if  $E$  is the lowest energy of the system, then  $E$  is a functional of the electron density only [1]:

$$E = F[n], \quad (30)$$

where the total energy,  $E$ , is of the many body Schrödinger equation defined as

$$E = \langle \Psi | \hat{H} | \Psi \rangle = \int d\mathbf{r}_1 \dots d\mathbf{r}_N \Psi^*(\mathbf{r}_1, \dots, \mathbf{r}_N) \hat{H} \Psi(\mathbf{r}_1, \dots, \mathbf{r}_N). \quad (31)$$

This is a remarkable result as generally the quantum state is a functional of the entire wave-function,

$\Psi(\mathbf{r}_1, \mathbf{r}_2, \dots, \mathbf{r}_N)$  containing  $3N$  variables. However, in this model, the ground-state energy depends only on  $n(\mathbf{r})$  which is a function of only 3 variables. One of the requirements of Eq.(30) is that in the ground state, the electron density uniquely determines the external potential of the nuclei,  $V_n$ . This can be demonstrated by *reductio ad absurdum* as done in Ref.[1]. It is done by starting from the assumption that the ground-state electron energy is obtained from two different external potentials which leads to a contradiction. By introducing the definition of the kinetic energy and Coulomb energy defined as

$$\hat{T} = - \sum_i \frac{1}{2} \nabla_i^2, \quad \hat{W} = \frac{1}{2} \sum_{i \neq j} \frac{1}{|\mathbf{r}_i - \mathbf{r}_j|}, \quad (32)$$

the functional can be written as

$$E = F[n] = \int d\mathbf{r} n(\mathbf{r}) V_n(\mathbf{r}) + \langle \Psi[n] \hat{T} + \hat{W} \Psi[n] \rangle. \quad (33)$$

The idea of Kohn and Sham was to split the final two terms into the kinetic and Coulomb energy of independent electrons as well as an extra term which accounts for the difference [14]. Eq.(33) then becomes

$$E = F[n] = \int d\mathbf{r} V_n(\mathbf{r}) - \sum_i \int d\mathbf{r} \phi_i^*(\mathbf{r}) \frac{\nabla^2}{2} \phi_i(\mathbf{r}) + \frac{1}{2} \int \int d\mathbf{r} d\mathbf{r}' \frac{n(\mathbf{r})n(\mathbf{r}')}{|\mathbf{r} - \mathbf{r}'|} + E_{xc}[n], \quad (34)$$

where the extra term,  $E_{xc}$ , is known as the exchange and correlation energy. It will be further discussed in Sec.II.H..  $E_{xc}$  contains everything that is left out and is done as the aim is to collect all the unknowns of the functional in one term and hope that it isn't too large. The final two terms in Eq.(29) are equal to the exchange and correction potential which is defined as

$$V_{xc}(\mathbf{r}) = \frac{\delta E_{xc}[n]}{\delta n}(\mathbf{r}). \quad (35)$$

A complete derivation is beyond the scope of this review however, it can be found in various textbooks such as Ref.[8].

## H. The Exchange and Correction Energy

For KS DFT, only the exchange-correction energy  $E_{xc} = E_x + E_c$  as a functional of the electron density needs to be approximated. The functional is often written as

$$E_{xc}[n] = \int n(\mathbf{r}) \epsilon_{xc}[n(\mathbf{r})] d\mathbf{r}. \quad (36)$$

Approximations of this functional typically fall into two categories: The Local Density Approximation (LDA) and The Generalised Gradient Approximation (GGA). The LDA assumes that the exchange–correction energy density at every position in space is the same as a uniform electron gas. This is expressed as

$$E_{xc}^{\text{LDA}}[n] = E_x^{\text{LDA}}[n] + E_c^{\text{LDA}}[n], \quad (37)$$

where

$$E_x^{\text{LDA}} = C \int n^{\frac{4}{3}}(\mathbf{r}) d\mathbf{r}. \quad (38)$$

The GGA is an improvement on the LDA which is also dependent on the gradient of the electron density and is expressed as

$$E_{xc}^{\text{GGA}}[n] = \int n(\mathbf{r}) \epsilon_{xc}[n(\mathbf{r}), |\nabla n(\mathbf{r})|] d\mathbf{r}. \quad (39)$$

The GGA is one of the most common approximations used in liquid water. Three examples of these include Perdew–Burke–Ernzerhof (PBE) functional [15] as well as the Becke–Lee–Yang–Parr (BLYP) functional [16][17] and the Becke–Perdew functional [15][18][19]. The derivation of these functionals are lengthy and thus will not be discussed in this review.

It is important for the XC functional to be as good of an approximation as possible for several reasons. As DFT gives direct access to the electronic charge distribution of a system, the correct interpretation of experimental observables such as infra-red spectra [20] [21], dielectric properties [22], x-ray scattering intensities [23] and surface potentials [24] are important (references extracted from Ref.[25]). More recent and accurate XC functionals known as Hybrid Functionals will be the topic of Sec.VI.D..



## I. The Kohn-Sham equations

Putting together all the previous section, the Kohn-Sham equations are re-written here as:

$$\left[ -\frac{\nabla^2}{2} + V_{\text{tot}}(\mathbf{r}) \right] \phi_i(\mathbf{r}) = \epsilon_i \phi_i(\mathbf{r}), \quad (40)$$

$$V_{\text{tot}} = V_{\text{n}}(\mathbf{r}) + V_{\text{H}}(\mathbf{r}) + V_{\text{xc}}(\mathbf{r}), \quad (41)$$

$$V_{\text{n}}(\mathbf{r}) = -\sum_I \frac{Z_I}{|\mathbf{r} - \mathbf{R}_I|}, \quad (42)$$

$$\nabla^2 V_{\text{H}}(\mathbf{r}) = -4\pi n(\mathbf{r}), \quad (43)$$

$$V_{\text{xc}}(\mathbf{r}) = \frac{\delta E_{\text{xc}}[n]}{\delta n}(\mathbf{r}), \quad (44)$$

$$n(\mathbf{r}) = \sum_i |\phi_i(\mathbf{r})|^2 \quad (45)$$

These Kohn–Sham equations describe the behaviour of non–interacting electrons in an effective local potential. For the exact functional and thus the exact local potential, the Kohn–Sham equations yield the exact ground state density from Eq.(45) and exact ground state energy first described in Eq.(1).

## J. Self Consistency

It is important to note that the first Kohn-Sham equation, Eq.(40), contains the potentials  $V_{\text{H}}$  and  $V_{\text{xc}}$  which depend on the electron density,  $n$ , and this electron density depends on the unknown eigenfunctions,  $\phi_i$ , via Eq.(45). This means that every solution  $\phi_i$  depends implicitly on all other solutions,  $\phi_j$ , describing the occupied electron state. The fact that all the solutions  $\phi_i$  are linked with each other via Eq. (40 - 45) implies that they must be solved self-consistently as was the case with the Hartree-Fock equations.

## III. Methods used to solve the Kohn-Sham equations

This section will highlight the most important tools that are used to solve the KS equations such as basis sets and pseudopotentials which are common tools in CPMD.

### A. Basis Sets: Gaussians and Slater Functions

For the KS equations to be solved computationally, a basis set is used to represent the orbitals,  $\phi_i$ , in terms of functions,  $f_\nu$ , with well known properties. Generally, a linear combination of basis functions

$$\phi_i(\mathbf{r}) = \sum_\nu c_{i\nu} f_\nu(\mathbf{r}) \quad (46)$$

are used where  $c_{i\nu}$  is a coefficient to be determined and  $f_\nu(\mathbf{r})$  is a basis function. There are two common local basis functions that are used. These are Slater-type basis functions (STOs) defined as

$$f_{\text{m}}^{\text{S}}(\mathbf{r}) = N_{\text{m}}^{\text{S}} r_x^{m_x} r_y^{m_y} r_z^{m_z} e^{-\zeta_{\text{m}} |\mathbf{r}|}, \quad (47)$$

with an exponential decaying radial part and Gaussian-type basis functions (GTOs) given as

$$f_{\text{m}}^{\text{G}}(\mathbf{r}) = N_{\text{m}}^{\text{G}} r_x^{m_x} r_y^{m_y} r_z^{m_z} e^{-\alpha_{\text{m}} r^2}, \quad (48)$$

where  $N_{\text{m}}$ ,  $\zeta_{\text{m}}$  and  $\alpha_{\text{m}}$  are constants that are kept fixed during the computation. Generally, STOs are more accurate but take longer to compute. This problem can be overcome as when a linear combination of enough GTOs are used, they approximate to STOs and use less computational time. Hence, GTOs are much more commonly used in software packages.

## B. Basis Sets: Plane Waves

A different approach to constructing a basis is possible by applying Bloch's Theorem. In a periodic system, the periodicity of the underlying lattice produces a periodic potential thus the electron density must also be periodic. For a periodic potential,  $V(\mathbf{r} + \mathbf{L}) = V(\mathbf{r})$ , where  $L$  is the length of the unit cell, the eigenfunctions can be written in the form

$$\phi_i(\mathbf{r}) = e^{i\mathbf{k}\cdot\mathbf{r}} u_{i\mathbf{k}}(\mathbf{r}), \quad (49)$$

where

$$u_{i\mathbf{k}}(\mathbf{r} + \mathbf{L}) = u_{i\mathbf{k}}(\mathbf{r}). \quad (50)$$

Hence the basis function,  $f_\nu(\mathbf{r})$ , in Eq.(46) using Bloch's Theorem can be written as

$$f_m^{\text{PW}}(\mathbf{r}) = N e^{i\mathbf{G}\cdot\mathbf{r}}, \quad (51)$$

where the normalization constant is defined as  $N = 1/\sqrt{\Omega}$  where  $\Omega$  is the volume of the periodic cell. Hence in this basis, the KS orbitals are defined as

$$\phi_j(\mathbf{r}, \mathbf{k}) = \frac{1}{\sqrt{\Omega}} \sum_{\mathbf{G}} c_j(\mathbf{G}, \mathbf{k}) e^{i(\mathbf{G}+\mathbf{k})\cdot\mathbf{r}}, \quad (52)$$

where  $c_j(\mathbf{G}, \mathbf{k})$  are complex numbers. In this basis, the charge density given by Eq.(45) can be written as

$$\begin{aligned} n(\mathbf{r}) &= \frac{1}{\Omega} \sum_j \int f_j(\mathbf{k}) \sum_{\mathbf{G}, \mathbf{G}'} c_j^*(\mathbf{G}', \mathbf{k}) c_j(\mathbf{G}, \mathbf{k}) e^{i(\mathbf{G}+\mathbf{k})\cdot\mathbf{r}} d\mathbf{k} \\ &= \sum_{\mathbf{G}} n(\mathbf{G}) e^{i\mathbf{G}\cdot\mathbf{r}}, \end{aligned} \quad (53)$$

where the sum over the  $\mathbf{G}$  vectors is over twice the range given by the wave function expansion. When the size of the system grows for atomic orbital basis sets, the number of functions needed to describe the system grows quadratically. However, there is only a linear dependence for plane waves which is the main advantage of this basis.

In actual calculations, the infinite sum over  $\mathbf{G}$  vectors in Eq.(53) is truncated to include only plane waves that have a kinetic energy smaller than some particular cutoff energy given by

$$\frac{1}{2} |\mathbf{k} + \mathbf{G}|^2 \leq E_{\text{cut}}, \quad (54)$$

where  $E_{\text{cut}}$  is given in Hartree units. The significance of this is that the number of plane waves is only determined by  $E_{\text{cut}}$  making it the only parameter that needs to be specified. One of several novel ideas of Ref.[3] was that  $V_H$  could be computed very efficiently using the plane wave basis. A fast Fourier transform (FFT) algorithm can be performed on Eq.(43) giving the expression

$$\nabla^2 \sum_{\mathbf{G}} V_H(\mathbf{G}) e^{-i\mathbf{G}\cdot\mathbf{r}} = 4\pi \sum_{\mathbf{G}} n(\mathbf{G}) e^{-i\mathbf{G}\cdot\mathbf{r}}. \quad (55)$$

Solving Eq.(55) gives the Hartree potential as

$$v_H(\mathbf{G}) = \frac{4\pi}{|\mathbf{G}|^2} n(\mathbf{G}). \quad (56)$$

A fast Fourier transformation can then be performed on Hartree potential to express it in real space. Using this method gives an algorithmic complexity of  $N \log N$ . If calculations are performed on a basis set of 50,000 plane waves then a FFT would lead to a calculation that is over 300 times faster.

## C. Pseudopotentials

To a certain degree, only the valence electrons participate in chemical bonding therefore, it is reasonable to replace the chemically inactive electrons by pseudopotentials. Each atom's nucleus and core electrons are modeled as an ions. As the core electrons are close to the nucleus, the valence electrons feel a weaker potential from the nucleus via a screening effect. Thus, the Coulomb potential near the nucleus is replaced with a modified weaker potential. This is what is known as a pseudopotential. Outside the core region,  $r_c$ , ideally, the pseudopotential gives an identical valence electron wavefunction. An example of a pseudopotential can be seen in Fig.2.

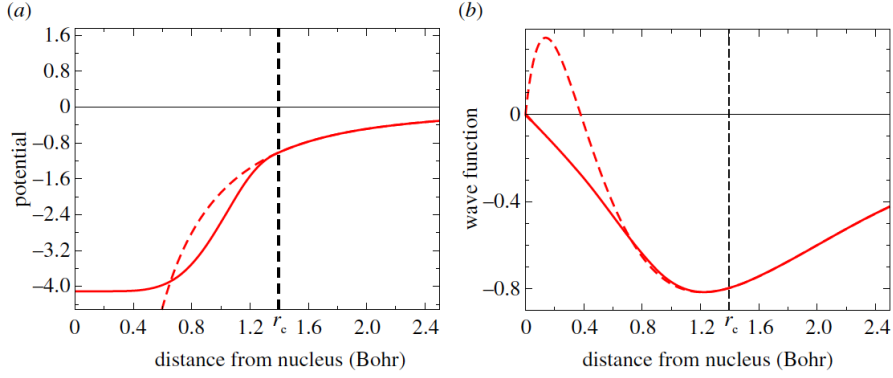


Fig. 2: (a): The Coulomb potential (dashed line) and an example pseudo-potential (solid line) for a carbon atom, along with the corresponding radial components of the 2s-orbital.(b): The potential and pseudopotential match beyond  $r_c$  as do the computed wave functions. Figure reproduced from Ref.[26].

Pseudopotentials are useful as it is unnecessary to describe the Kohn-Sham wavefunction of core states and so faster calculations and the simulation of larger systems are possible. For example, for the element tungsten only six valence electrons need to be described as opposed to a total of 74 electrons. Another advantage of incorporating pseudopotentials is that many of the relativistic effects are connected to the core electrons. As relativistic equations aren't used to derive the Kohn-Sham equations, the relativistic effects can be incorporated into an accurate pseudopotential without complicating the calculations of the final system. The use of pseudopotentials is what makes it possible to study complex systems involving many atoms. A more in-depth description of pseudopotentials and their application within the framework of basis sets can be found in many AIMD textbooks such as Ref.[27].

#### D. Numerical solution of the Kohn-Sham equations

The procedure for solving the KS equations, Eq.(40-45), is to first specifying the nuclear coordinates such that  $V_n$  can be calculated in Eq.(42). The nuclear coordinates are available from crystallography data. Typically however,  $V_n$  is replaced by a pseudopotential which is the topic of Sec.III.C..

A first guess for the electron density,  $n(\mathbf{r})$ , is then made to determine a preliminary approximation to the Hartree and the Exchange and Correction potential. This can be done by adding up the densities corresponding to completely isolated atoms arranged in the atomic position that is specific to the material under consideration. An example of how the Hartree potential,  $V_H$ , is calculated in the plane wave basis is briefly discussed in Sec.III.B.. The Exchange and Correction potential,  $V_{XC}$ , was also previously mention in Sec.II.H. where relevant literature had been highlighted. The total potential is then calculated using Eq.(41). Eq.(40) is then solved numerically which is possible in a variety of ways. One of which by discretizing space into a mesh of points and also using finite difference formulas to replace the Laplace operator. By solving this equation, new wavefunctions,  $\phi_i$ , are obtained which can be used to constructs a better estimate of the electron density,  $n$ , via Eq.(45). Thus, a better estimate of the total potential  $V_{tot}$  can be obtained. The process is then repeated until a the density matches the previous iteration of the density calculation within a specified tolerance at which self-consistency is said to be obtained. This procedure is illustrated in Fig.3.

Once the desired electron density in the ground staten( $\mathbf{r}$ ) is obtained, the total energy  $E$  of the system can be calculated using Eq.(34).

### IV. Car-Parrinello Molecular Dynamics

The Car-Parrinello equations of motion are derived in this section. There will also be a brief outline of why the Car-Parinello method works.

#### A. The Car-Parrinello Lagrangian and equations of motion

Prior to the publication of Ref.[3] in 1985, the computational bottleneck involved the converging of electronic wave-functions at every step. This problem was solved by artificially introducing classical coupling between the decoupled electronic and nuclear degrees of freedom. It takes advantage of the quantum-mechanical adiabatic

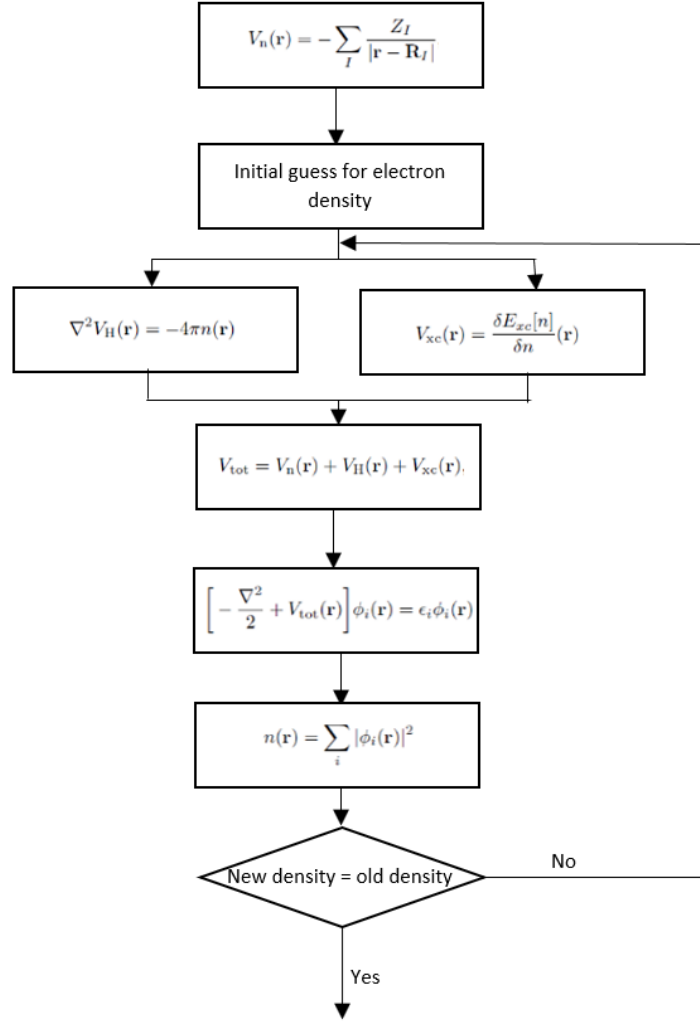


Fig. 3: Flow chart illustrating how the KS equations are solved to find  $n(\mathbf{r})$ . The equality in the conditional symbol indicates when the previous iteration of the density is within a specified tolerance of the new density. Figure reproduced from Ref.[8].

time scale of slow (classical) nuclear and fast electron (quantum) motion. This is achieved by transforming the separation into a classical mechanic adiabatic energy scale separation in the framework of dynamical theory [27]. The two component quantum classical problem is mapped to a two component purely classical problem with two energy scales. However, this comes at the expense of losing the physical time information of the quantum subsystem dynamics. the energy of the electronic subsystem,  $\langle \Psi_0 | \mathcal{H} | \Psi_0 \rangle$ , is a function of nuclear position,  $\mathbf{R}_I$ , as well as a function of the wave function,  $\Psi_0$ , and thus a set of orbitals,  $\phi_i$ , can be used to build the wave-function. As with classical physics, a functional derivative with respect to the orbitals, which can be interpreted as classical field of an accurately defined Lagrangian may give the correct force on the orbitals. Certain constraints must also be imposed on the orbitals such as orthonormality. Car and Parrinello introduced the following type of Lagrangians [3]:

$$\mathcal{L}_{\text{CP}} = \sum_I \frac{1}{2} M_I \dot{\mathbf{R}}_I^2 + \sum_i \mu \langle \dot{\phi}_i | \dot{\phi}_i \rangle - \langle \Psi_0 | \mathcal{H} | \Psi_0 \rangle + \text{constrains}, \quad (57)$$

where the first two terms represent the kinetic energy, the third term represents the potential energy and the fourth term is due to orthonormality. There is also a pre-factor of  $\mu_i/2$  which is sometimes included which allows orbital occupation numbers  $f_i = 0, 1, 2$  to be introduced. The equations of motion can be found by solving the two Euler-Lagrange equations given as

$$\frac{d}{dt} \frac{\partial \mathcal{L}}{\partial \dot{\mathbf{R}}_I} = \frac{\partial \mathcal{L}}{\partial \mathbf{R}_I}, \quad (58)$$

$$\frac{d}{dt} \frac{\delta \mathcal{L}}{\delta \dot{\phi}_i^*} = \frac{\delta \mathcal{L}}{\delta \phi_i^*}, \quad (59)$$

for both the nuclear position and orbitals. For Eq.(59), the functional derivatives have to be taken with respect to the orbitals,  $\phi_i(\mathbf{r})$ , which are complex scalar fields. By solving the Euler-Lagrange equations, the generic Car-Parrinello equations of motion are of the form

$$M_I \ddot{\mathbf{R}}_I(t) = -\frac{\partial}{\partial \mathbf{R}_I} \langle \Psi_0 | \mathcal{H}_e | \Psi_0 \rangle + \frac{\partial}{\partial \mathbf{R}_I} \{\text{constraints}\}, \quad (60)$$

$$\mu \ddot{\phi}_i(t) = -\frac{\delta}{\delta \phi_i^*} \langle \Psi_0 | \mathcal{H}_e | \Psi_0 \rangle + \frac{\delta}{\delta \phi_i^*} \{\text{constraints}\}, \quad (61)$$

where  $\mu$  is the inertia parameter assigned to the orbital degrees of freedom with the units [E][t<sup>2</sup>]. The total ground state of an interacting system of electrons with classical nuclei that are fixed at positions,  $\mathbf{R}_I$ , is defined as

$$E_{\text{tot}} = \min_{\Psi_0} \{ \langle \Psi_0 | \mathcal{H}_e | \Psi_0 \rangle \} = \min_{\{\phi_i\}} E^{\text{KS}}[\{\phi_i\}], \quad (62)$$

where

$$\min_{\{\phi_i\}} E^{\text{KS}}[\{\phi_i\}], \quad (63)$$

is the minimum of the Kohn-Sham energy. The Kohn-Sham energy is defined as

$$E^{\text{KS}}[\{\phi_i\}] = T_S[\{\phi_i\}] + \int V_{\text{ext}}(\mathbf{r}) n(\mathbf{r}) d\mathbf{r} + \frac{1}{2} \int V_H(\mathbf{r}) n(\mathbf{r}) d\mathbf{r} + E_{\text{XC}}[n], \quad (64)$$

which is an explicit functional of the functions,  $\{\phi_i(\mathbf{r})\}$ , which are the Kohn-Sham orbitals that satisfy the relation  $\langle \phi_i | \phi_j \rangle = \delta_{ij}$  [1]. For the special case of the effective one particle Hamiltonian such as one resulting from Kohn-Sham theory, as well as using the position-independent constraints, the Lagrangian simplifies to

$$\mathcal{L}_{\text{CP}} = \sum_I \frac{1}{2} M_I \dot{\mathbf{R}}_I^2 + \sum_i \mu \langle \dot{\phi}_i | \dot{\phi}_i \rangle - \langle \Psi_0 | \mathcal{H}_e^{\text{KS}} | \Psi_0 \rangle + \sum_{i,j} \Lambda_{ij} (\langle \phi_i | \phi_j \rangle - \delta_{ij}), \quad (65)$$

where  $\langle \phi_i | \phi_j \rangle = \delta_{ij}$  must be imposed by the Lagrange multipliers  $\Lambda_{ij}$ . By solving the Euler Lagrange equations given by Eq. (58) and (59) the Car-Parrinello equations of motion are given as

$$M_I \ddot{\mathbf{R}}_I(t) = -\nabla_I \langle \Psi_0 | H_e^{\text{KS}} | \Psi_0 \rangle, \quad (66)$$

$$\mu \ddot{\phi}_i(t) = -H_e^{\text{KS}} \phi_i + \sum_j \Lambda_{ij} \phi_j. \quad (67)$$

Using the methods described in Sec. III., these equations of motion can be solved using software packages such as CPMD and CASTEP for various systems. The application of CPMD will be discussed in Sec.V. and Sec.VI..

## B. Why the Car-Parrinello method works

Ref.[28], published in 1991 examining some of the theoretical issues underlying the Car-Parrinello method. The dynamics of the Car-Parrinello Lagrangian defined in Eq.(57) in particular were analyzed and the paper showed that the CP dynamics of the electronic variables consisted of small oscillations whose eigenfrequencies are approximately given by the differences between eigenvalues of the effective Schrödinger equation. This was done by making the connection with the “averaging method” [29] in classical mechanics. Thus, the oscillation dynamics makes it possible to approximate the desired Born-Oppenheimer (BO) dynamics of the ionic system.

Because of the large mass difference between ions and electrons, there is a separation between the time scales of their motion. The electrons have enough time to readjust and thus follow the slow ionic movement. Due to this, the “averaging method” works as the intrinsic high-frequency motion of the electronic variables has the consequence that the electronic degrees of freedom are allowed to follow the slow evolution of the ionic variables. This is why the Hamiltonian of a system containing fast and slow variables can be approximated to an “averaged” Hamiltonian which is obtained by performing an average of the fast coordinates in the original Hamiltonian.

Evidence of this is also presented in the paper. A very simplified material of bulk crystalline silicon with an *fcc* elementary cell of length 10.26 a.u and a diamond-like basis of two Si atoms is considered. If the KS

Hamiltonian were a linear operator, the dynamics of the orbitals would have harmonic modes with frequencies equal to

$$\omega_{ij} = \left( \frac{\epsilon_i - \epsilon_j}{\mu} \right)^{1/2}, \quad (68)$$

where  $\epsilon_i$  and  $\epsilon_j$  are the eigenvalues of the occupied and unoccupied orbital defined in Eq.(29). The vibrational density of states of this system is included in Fig.4. It is the Fourier transformation of the statistically averaged velocity auto-correlation function of the Fourier coefficients of the KS orbitals defined as

$$f(\omega) = \int_0^\infty \cos(\omega t) \sum_i \langle \dot{\phi}_i; t | \dot{\phi}_i; 0 \rangle dt, \quad (69)$$

where the time average is performed over 3000 time steps. From the figure, it is evident that for the parameters

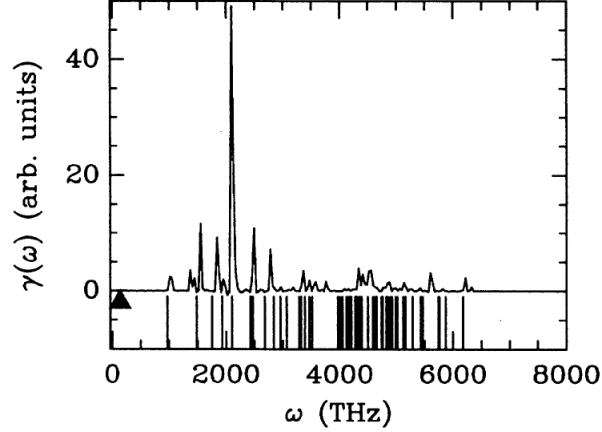


Fig. 4: Vibrational spectrum of the normal modes of the electronic degrees of freedom for the two Si system described. The solid triangle is located at the position of the highest ionic frequency. The vertical bars below the spectrum are obtained using Eq.(68). Figure reproduced from Ref.[28].

chosen, the electronic and nuclear subsystem are both dynamically separated as their power spectra do not overlap. Due to this energy gap, between the highest phonon frequency and lowest orbital frequency, the energy transfer from hot nuclei to the cold electrons is particularly slow. The figure also justifies how the Hamiltonian can be “averaged” and why the Car-Parrinello method is an effective approximation.

## V. Application of Density-Functional Theory

Now that the background of DFT has been introduced, this section will highlight various application of DFT. All the papers in this section that have been selected implement CPMD.

### A. Semiconductor Photocatalysis

Pervoskite solar cells are a type of low cost solar cell that increased in efficiency from 3.8% in 2009 to 22.1% in 2016 thus making the technology an interesting field of research. Semiconductor Photocatalysis receives a lot of attention as a possible solution for counteracting environmental degradation and easing the worldwide energy shortage. It has emerged as a promising solution as it utilizes the energy of either sunlight or artificial indoor which is abundantly available. Photocatalysis has a wide range of potential applications in a large range of fields. Some of which include: artificial photosynthesis, photo-decomposition or photo-oxidization of hazardous substances and photo-induced super-hydrophilicity [30].

As photo-catalytic reactions take place on the catalyst surface, DFT can be used to investigate how the target molecules behave on the surface. A brief summary of some of the properties of water molecule adsorption properties of photo-catalyst surfaces using CPMD will be highlighted. A snapshot of the (010) surface of a  $\text{YVO}_4$  catalyst, upon which adsorbed water molecules are in thermal equilibrium at 300 K is included in Fig.5. A Good performance in the evolution of both  $\text{H}_2$  and  $\text{O}_2$  were observed in experiments performed under UV light irradiation in Ref.[31]. The  $\text{YVO}_4$  crystal contained two kinds of polyhedra: a  $\text{VO}_4$  tetrahedron and a  $\text{YO}_8$  triangular dodecahedron at which no absorption was observed on both these sites. The water absorption

properties of  $\text{YVO}_4$  such as the adsorption energy for the 7c-Y site being 0.64 eV/molecule were also calculated in Ref.[32]. From this brief review, what is important to conclude is that CPMD can be used to predict absorption properties of Semiconductor Photocatalysis such as  $\text{YVO}_4$  which can further the understanding of materials within the field.

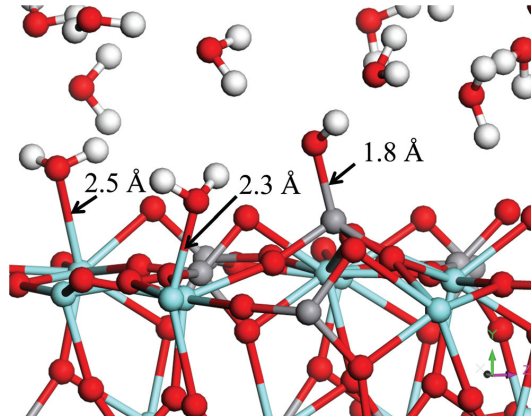


Fig. 5: A snapshot of the (010) surface of the  $\text{YVO}_4$  catalyst with absorbed water molecules in thermal equilibrium at 300 K. The grey, sky blue, red and white spheres representing Vanadium, Yttrium, Oxygen and Hydrogen respectively. Figure reproduced from Ref.[32].

## B. Simulations of Methylammonium Lead Iodide Perovskite Degradation by Water

The protection of organohalide perovskite thin films from water and humidity is of significance for the commercial uptake of perovskite solar cells. Because of this, understanding the perovskite–water interface is of crucial importance for the perovskite solar cell industry which can be achieved using AIMD simulations. In particular, the interaction between the methylammonium lead iodide ( $\text{MAPbI}_3$ ) perovskite surfaces and a liquid water environment were studied in Ref.[33]. This was used to analyze the degradation process that perovskite may undergo in the presence of liquid water. It was concluded that MAI–terminated slabs undergo rapid solvation which is driven by the interaction of water molecules with Pb atoms prompting the release of I atoms. The authors also concluded that the work unraveled atomic details of the perovskite– $\text{H}_2\text{O}$  interface may inspire new interfacial modifications and device architectures with increased stability. This in turn could then further assist in the widespread uptake of perovskite solar cells.

## C. Biological Systems: Prions

In this section, a few examples of CP applications to biological systems of interest will be presented. The first being the binding of copper ions to the murine prion protein which gives insight into the nature of transition metal–protein interactions that would otherwise be difficult to capture [34]. Prions are a type of infectious agent responsible for several neurodegenerative diseases that affect animals such as sheep (scrapie), cattle (BSE), and humans (Creutzfeldt-Jacob disease). It is well established that these diseases are caused by an abnormal isoform  $\text{PrP}^{\text{Sc}}$  of the normal cellular prion protein  $\text{PrP}^{\text{C}}$  [35]. Experiments both *in vitro* and *in vivo* indicate that prions are able to bind to metal ions such as  $\text{Cu}^{2+}$  [36]. Identifying the copper binding sites in the structured part of prion proteins as well as the metal protein interactions are of great interest. This is because it has been suggested that metal ions could influence the structural stability and also the transition to the infectious scrapie form. Furthermore, there is substantial evidence that interaction with metal ions plays a crucial role in other neurodegenerative disorders such as Alzheimer’s [37] and Parkinson’s [38].

Simulations with the aim of identifying likely locations for  $\text{Cu}^{2+}$  bindings were performed using CPMD in Ref.[39]. Characteristic snapshots of one of the dynamics runs is shown in Fig.6 which illustrates the complex and dynamical nature of the metal binding properties.

## D. Biological Systems: HIV-1 Protease Cleavage Site

The simulation of the bond breaking and forming process that occurs in chemical reactions can be studied by considering the electronic degrees of freedom. It can be used to study enzymatic mechanisms of protease from

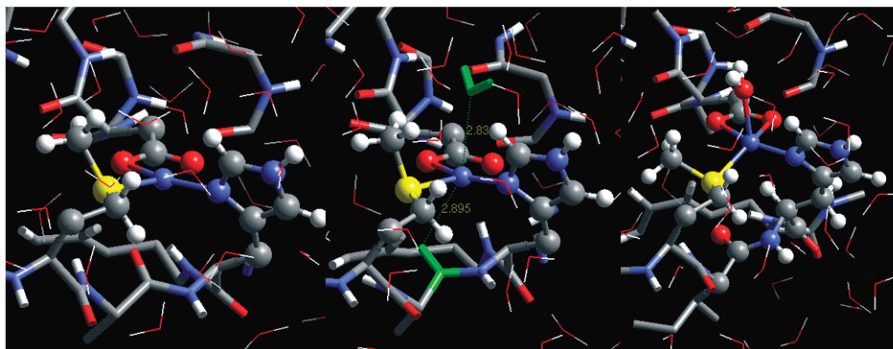


Fig. 6: A sequence of snapshots from a CP simulation of a potential  $\text{Cu}^{2+}$  binding site in the mouse prion protein. The quantum mechanical part is shown in cylinders and the classical environment is given a stick representation. The copper ion is shown in yellow. The length of the simulation is around 5 ps. Of significance are the dynamical changes that occur in the copper coordination sphere. Figure reproduced from Ref.[39].

the human immunodeficiency virus type 1 (HIV-1 PR) which is a prime target for drug therapy. The cleavage site consists of two aspartyl residues known as Asp25 and Asp25'. Previous studies using force-field-based MD encountered difficulty when describing the conformational properties of the cleavage site which is critical to understand for drug binding. CPMD simulations on models of the active site were used to give a better understanding of the molecular interactions between the Asp pair were conducted in Ref.[40]. The calculations suggested that the close proximity of the cleavage site is achieved by the formation of a low barrier hydrogen bond (LBHB) which is illustrated in Fig.7.

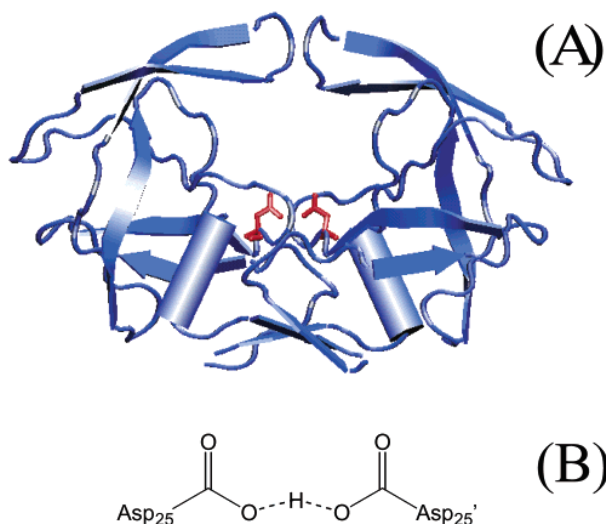


Fig. 7: A) A three-dimensional structure of HIV-1 PR which is essential for the virus' metabolism. The Asp catalytic dyad is in red. B) The LBHB between the Asp pair in the free enzyme which was obtained by the CPMD simulation on the model system. Figure reproduced from Ref.[40].

## VI. The Structure of Water

Liquid water is a particularly popular system that is studied using computational methods. This section will focus on research involving CPMD simulations of liquid water using density functional theory in the Kohn-Sham formulation. This section will highlight the application of CPMD on the structure of water. First there will be a brief overview of the field in Sec.VI.A. and then more recent research on larger simulations will be discussed in Sec.VI.B.. The diffusion of water will then be discussed in Sec.VI.C. which is of importance in the conclusion and finally, recent papers that improve upon the XC-functional will be reviewed in Sec.VI.D..



## A. Computational papers

The first Car-Parrinello simulation of bulk liquid water paper titled *Ab initio* liquid water was published in 1993 by K. Laasonen et al [41]. A plane wave base set (discussed in Section III.B.) was used to determine the electronic structure and forces at each step. The CP method was used giving the equations of motion of the system that were previously defined in Eq (66-67) in Section IV.A..

A system of 32 D<sub>2</sub>O molecules contained in a cubic cell of length 9.6 Å at room temperature with periodic boundary conditions was simulated. The time step for the simulation was chosen to be 0.169 fs and  $\mu = 1100$  a.u. was set for the parameter in the Lagrangian. These large choices for the the time step and  $\mu$  were the reason D<sub>2</sub>O was simulated as opposed to ordinary water. A simulation was performed using only the exchange corrections of the Becke gradient corrections (GC) density functional (GC density functionals briefly discussed in Section II.H.). The results for the pair correlation were then plotted and compared with experimental data which can be seen in Fig.8. The results were particularly encouraging and show that the CP method was suitable to treating aqueous solutions.

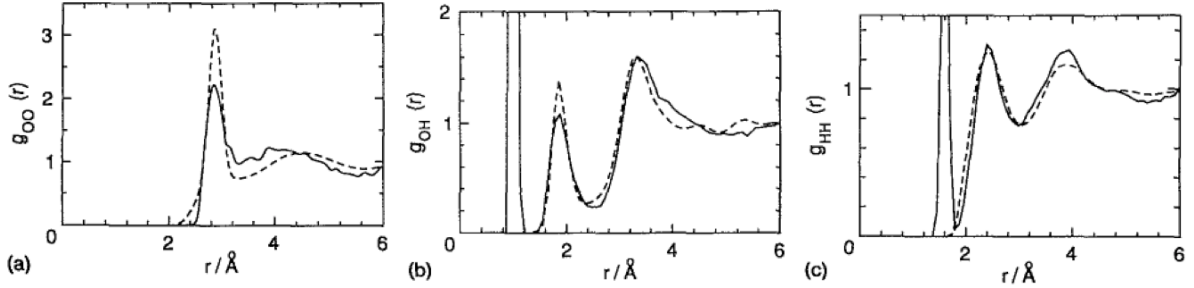


Fig. 8: The partial radial distribution of water. The solid line represents the results of the AIMD simulation with the Becke gradient correction for exchange only. The dashed lines are results used from a previous experiment for comparison to the simulation [42]. Figure reproduced from [41].

Since Ref. [41], there have been a number of studies using the CP method to simulate liquid water. One of these includes a paper written by Michiel Sprik et al. [43]. It compared three commonly used gradient-corrected density functionals (B, BP, BLYP) applied to AIMD simulation of liquid water to evaluate their performance. It was found that the (BLYP) density functional yielded the best agreement with experiment.

The first 64 molecule simulation was published in 1995 by P. Silvestrelli and M. Parrinello [44]. It reported the results of an AIMD simulation of liquid water with a system of twice as many water molecules compared to previous AIMD simulations. The system consisted of a 64 molecule supercell with body-centred-cubic symmetry at constant volume and at room temperature and a BLYP density functional. The oxygen oxygen pair correlation functions were compared to experimental data as can be seen in Fig.9. The 64 molecule system is a better fit to experimental data.

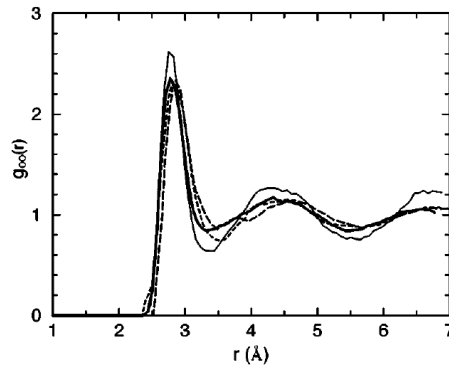


Fig. 9: Oxygen-oxygen pair correlation functions of radius from AIMD simulation (thick solid line for the 64 molecule system and solid line for 32- molecule system) in compared to experimental neutron scattering Ref.[45] (dashed line) and x-ray diffraction Ref.[46] (long dashed line). Figure reproduced from Ref.[44].

Some of the *ab initio* simulations in these papers showed significant disagreement with experiment and with each other. Thus, a papers titled The influence of temperature and density functional models in *ab initio*

molecular dynamics simulation of liquid water by J. VandeVondele et al. was published in 2005 [47]. To summarize, it investigated why there were discrepancies between simulations by running various simulations and changing various variables such as temperature to see the effect on parameters such as the total energy of the system.

There were a total of 16 simulations of 20 ps in the temperature range of (280 – 380) K which were used to determine the effect of temperature on the structure and dynamics of liquid water. For this simulation, the wave functions were represented using Gaussians and the density was expanded in an auxiliary basis of plane waves.

For the first experiment conducted, 16 systems were set up with a different total energy with all other parameters kept the same and the total energy chosen such that the final average temperatures were in the range of (280 – 380) K. This was then plotted as seen in Fig.10. The relationship between the total energy and temperature is effectively linear. The maximum fluctuation from the fitted line is on the order of 10 K which can be considered statistical uncertainty for the configuration of 32 water molecules and a 20 ps duration.

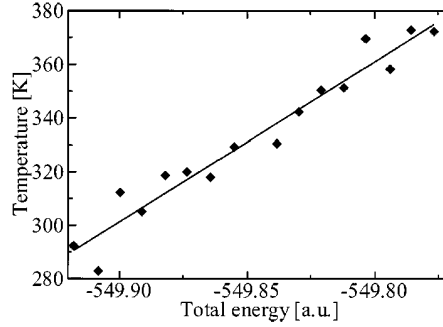


Fig. 10: Relationship between the total energy and the average temperature for 16 simulations with a linear fit. Figure reproduced from Ref.[47].

The resulting oxygen-oxygen pair correlation functions were also plotted as a function of distance. This can be seen in Fig.11. The change in the shape of the curves reflects the strong effect of temperature on the structure of water. The temperature dependence of the features of the curve such as the heights and position of the maxima and minima is in agreement with the expectation that the curves smooth when the temperature is increased. The maxima and minima also become less pronounced and positions of the first peak shifts outwards for increasing temperatures.

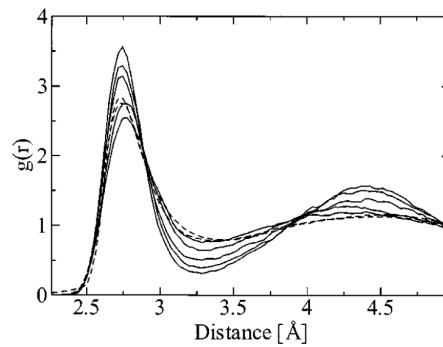


Fig. 11: 5 of the 16 oxygen-oxygen pair correlation functions corresponding to simulations of temperatures 292, 318, 329, 351 and 372 K. The three solid lines that are nearly indistinguishable are simulations with three unit cells of length 12.40, 12.42 and 12.44 Å. Figure reproduced from Ref. [47].

The oxygen-oxygen pair correlation functions were also plotted for four simulations of 64 and 32 water molecules which is included in Fig.12. As can be seen in Fig.12, the changes in the size of the unit cell have a small effect on the structure of water. There is also a relatively good agreement between the simulation for different particle numbers thus the size effects are small. The temperature dependencies observed for 32 molecules also carry over to 64 water molecules.

To conclude, the paper found that temperature has a strong influence over the structure and dynamics of liquid water whereas system size was found to be a comparatively less sensitive variable. Therefore a small variation in temperature may be the reason why the various previous papers using AIMD sometimes showed

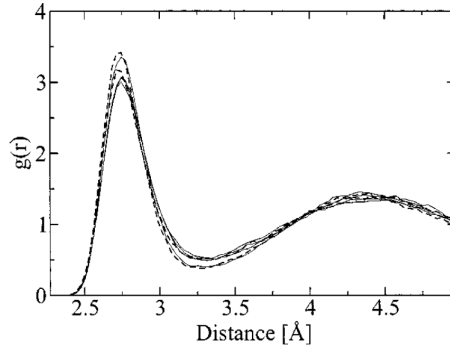


Fig. 12: Oxygen-oxygen pair correlation functions for four simulations of 64 water molecules (solid lines) and 32 water molecules (dashed lines). Figure reproduced from Ref. [47].

disagreement with each other as well as with experiments. In a separate paper, it was found that there were negligible differences in the structural properties of room temperature liquid obtained using the PBE or the BLYP functionals. Size effects, although not fully negligible when using 32 molecule cells, were also found to be rather small [48].

## B. Larger simulations

A much large simulation of large cells of up to 256 molecules investigating the electronic properties of water at ambient conditions using *ab initio* molecular density functional theory using the generalized gradient approximation was also investigated in Ref.[49]. The electronic degrees of freedom (EDOS) computed using a 32-molecule supercell with a single  $k$ -point was found to not be an accurate representation of the EDOS computed using a 256 molecule supercell with one  $k$ -point. This is due to liquid water not having a periodic structure. However, the EDOS computed using a 32 molecule system with eight  $k$ -points was found to be an accurate approximation of the EDOS of a 256 molecule supercell with one  $k$ -point.

This was shown by taking ten uncorrelated molecular configurations of 32 water molecules of liquid water at ambient conditions at intervals of 20 ps from a TIP4P model. A DTF electron structure calculations were performed increasing the  $k$ -point sampling of the first Brillouin zone. It was seen that 64  $k$ -points is sufficient to converge the EDOS of a larger system. Some of these convergence tests are included in Fig.13.

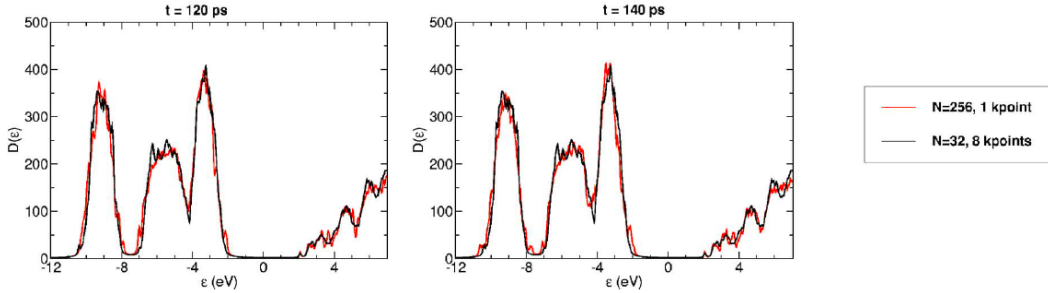


Fig. 13: Comparison of EDOS of liquid water for a 256 molecule supercell sampled every 20 ps at  $T = 300$  K and  $\rho = 0.996$  g/cm<sup>3</sup> and a 32 molecule supercell computed using eight  $k$  points in the first Brillouin zone. Figure reproduced from Ref.[49].

## C. The diffusion of water

A series of CPMD simulations were carried out in Ref.[50] for H<sub>2</sub>O and D<sub>2</sub>O investigate various properties of water at ambient conditions. The diffusion coefficient was computed using the Einstein relation given as

$$6D = \lim_{t \rightarrow \infty} \frac{d}{dt} \langle |\mathbf{r}_i(t) - \mathbf{r}_i(t_0)|^2 \rangle, \quad (70)$$

where  $\langle |\mathbf{r}_i(t) - \mathbf{r}_i(t_0)|^2 \rangle$  is the mean square displacement (MSD) and  $D$  is the diffusion coefficient. The slope of MSD as a function of simulation time was determined in the range of 1 – 10 ps and thus  $D$  was computed using Eq.(70). The results are included in Table 1 along with the peak positions of  $g(r)$ .

Table 1: For each simulation performed, the number of molecules  $N$  (32 or 54), molecule type ( $\text{H}_2\text{O}$  or  $\text{D}_2\text{O}$ ), density functional employed (PBE or BLYP), fictitious mass parameter  $\mu$  (a.u.), diffusion coefficient  $D$  ( $\text{cm}^2/\text{s}$ ), position ( $\text{\AA}$ ), and value of first maximum and minimum in the  $g(r)$  and average coordination (CN) of the water molecules are listed. For each calculation, quantities are averaged over the entire production run. The last two rows contain measured diffusion coefficients and structural data for water at ambient conditions. Table reproduced from Ref.[50].

$N$	Molecule	DFT	$\mu$	$D$	$R[g(r)_{\text{max}}]$	$g(r)_{\text{max}}$	$R[g(r)_{\text{min}}]$	$g(r)_{\text{min}}$	$T_{\text{avg}}$	Coordination
32	$\text{H}_2\text{O}$	PBE	340	$1.2 \times 10^{-6}$	2.71	3.46	3.30	0.41	290.8	4.3
32	$\text{H}_2\text{O}$	PBE	760	$3.1 \times 10^{-5}$	2.75	2.62	3.45	0.71	285.9	4.9
32	$\text{H}_2\text{O}$	BLYP	340	$1.1 \times 10^{-6}$	2.73	3.65	3.32	0.40	292.9	4.4
32	$\text{H}_2\text{O}$	BLYP	760	$2.3 \times 10^{-5}$	2.76	2.59	3.52	0.75	281.3	4.9
32	$\text{D}_2\text{O}$	PBE	340	$1.6 \times 10^{-6}$	2.72	4.11	3.30	0.35	294.7	4.2
32	$\text{D}_2\text{O}$	PBE	760	$1.5 \times 10^{-6}$	2.75	3.46	3.35	0.48	293.0	4.4
32	$\text{D}_2\text{O}$	BLYP	340	$5.5 \times 10^{-7}$	2.73	3.60	3.33	0.39	297.5	4.3
32	$\text{D}_2\text{O}$	BLYP	760	$1.5 \times 10^{-6}$	2.74	3.46	3.34	0.42	291.4	4.3
32	$\text{D}_2\text{O}$	BLYP	1100	$1.0 \times 10^{-5}$	2.77	2.84	3.46	0.66	283.9	4.8
54	$\text{H}_2\text{O}$	PBE	340	$3.7 \times 10^{-6}$	2.71	3.27	3.32	0.46	294.5	4.3
Exp.	$\text{H}_2\text{O}$	—	—	$2.2 \times 10^{-5}$	2.73	2.75	3.36	0.78	298.0	4.7 <sup>c</sup>
Exp.	$\text{D}_2\text{O}$	—	—	$1.8 \times 10^{-5}$	—	—	—	—	298.0	—

It was concluded that the diffusion coefficients of the  $\text{H}_2\text{O}$  and  $\text{D}_2\text{O}$  simulations fell into one of two categories depending on the value of  $\mu$ . Specifically for  $\mu = 760$  a.u.,  $D$  is in rather good agreement with the experimental value of  $2.4 \times 10^{-5} \text{ cm}^2/\text{s}$  for  $\text{D}_2\text{O}$ . However, for  $\mu = 340$  a.u.,  $D \sim 1 \times 10^{-6} \text{ cm}^2/\text{s}$  is smaller than the experimental value. It is also important to note that the value of  $D$  were almost equivalent when either the BLYP or PBE functionals were used. It was also noted that the discrepancy from the  $54\text{H}_2\text{O}$  compared to the  $34\text{H}_2\text{O}$  could have arisen from size effect or a different averaging time. Finally, when a large value of  $\mu$  such as  $\mu = 1100$  a.u., the value of  $D$  is in reasonable agreement with experimental measurements. However, when smaller values of  $\mu$  such as  $\mu = 320$  or  $760$  a.u., the simulated  $D$  are 10 – 20 times smaller.

The same research group also published a second paper in the same year to further understand some of the discrepancies previously mentioned [51]. This time, only  $\text{H}_2\text{O}$  was simulated with the PBE functional being used and the fictitious mass set to 340a.u. for most of the simulations. The data is included in Table 2 so that conclusions can be drawn from it.

Table 2: For each simulation performed, the type of simulation (CP or BO), number of molecules  $N$ , total simulation time (ps), average temperature ( $K$ ), diffusion coefficient  $D$  ( $\text{cm}^2/\text{s}$ ), position ( $\text{\AA}$ ), and value of first maximum and minimum in the  $g(r)$  and average coordination (CN) of the water molecules are listed. All the simulations are for  $\text{H}_2\text{O}$  with the PBE density functional used. The fictitious electron mass set to 340a.u. for flexible water or 1100a.u. for rigid water. The last two rows contain measured diffusion coefficients and structural data for water at ambient conditions. Table reproduced from Ref.[51].

Simulation	Type	$N$	Time	$T_{\text{ave}}$	$D$	$R[g(r)_{\text{max}}]$	$g(r)_{\text{max}}$	$R[g(r)_{\text{min}}]$	$g(r)_{\text{min}}$	CN
1	CP	54	19.8	296	$2.4 \times 10^{-6}$	2.69	3.65	3.32	0.37	4.2
2	CP	54	18.8	345	$5.0 \times 10^{-6}$	2.72	3.21	3.35	0.42	4.3
3	CP	54	22.0	399	$2.2 \times 10^{-5}$	2.75	2.60	3.41	0.73	4.6
4	BO	64	20.5	306	$7.9 \times 10^{-7}$	2.72	3.83	3.25	0.33	4.1
5	BO	64	20.7	349	$3.3 \times 10^{-6}$	2.72	3.49	3.30	0.40	4.2
6	BO	64	18.6	393	$1.2 \times 10^{-5}$	2.73	3.10	3.40	0.56	4.6
7	BO	64	10.5	442	$3.9 \times 10^{-5}$	2.75	2.63	3.44	0.74	4.8
8	CP-Rigid	54	24.5	315	$1.3 \times 10^{-5}$	2.75	2.92	3.41	0.61	4.6
9	CP-Rigid	54	26.3	345	$3.3 \times 10^{-5}$	2.75	2.61	3.41	0.77	4.7
10	TIP5P(PIMC), $P=1$	64	500.0	300	$2.6 \times 10^{-6}$	2.69	3.61	3.29	0.43	4.1
11	TIP5P(PIMC), $P=1$	64	500.0	350	$2.8 \times 10^{-5}$	2.72	2.84	3.38	0.78	4.6
12	TIP5P(PIMC), $P=5$	216	...	300	...	2.73	2.76	3.44	0.77	...
	Experiment	...	...	298	$2.3 \times 10^{-5}$	2.73	2.75	3.36	0.78	4.7

As can be seen in Table 2, the computed diffusion coefficients obtained in both CP and BO simulations at 300 K are smaller (by at least a factor of 10) compared to  $D$  measured experimentally at the same temperature in Ref.[52]. Also, the difference between the simulated and measured diffusion coefficients is statistically meaningful whereas, the difference between the CP and BO diffusion coefficients at 300K is not. In order to make quantitative comparison between diffusion the coefficients, orders of magnitude longer simulation times would be required.

Nonetheless, a variety of possible explanations were put forward to explain the discrepancy, the first being the accuracy of the exchange and correction functional used. A common shortcoming is the oxygen-oxygen distance in the LDA water dimer calculation which is much too short using common GGA approximations such as the PBE and BLYP functionals. A solution to this is discussed in Sec.VI.D. where hybrid functionals are introduced.

The second cause of discrepancy is the negligence of proton quantum effects as at 300K, the quantum and classical system will be qualitatively different in terms of the distribution of the vibrational energy of the system. The proton quantum effect can be accounted for using Monte Carlo sampling methods however, these will not be further discussed in this review.

AIMD simulations are typically limited to relatively short timescales of around 10 – 20 ps which can have a significant effect on the time interval of averages such radial distribution functions are taken. The limited time scales can also strongly influence dynamical properties such as computed diffusion coefficients.

Temperature also has a large effect when simulating water. The main structural changes that occur when going from a classical to a quantum description of water at 300 K can be approximated by increasing the temperature of classical simulations by 50 K. A model of TIP5PP(PIMC) was considered where TIP5P is a five site water model and TIP5P(PIMC) is a variant of this used in path integral simulations. The 50 K temperature increase also causes the diffusion coefficient of classical TIP5P(PIMC) water to increase from  $2.2 \times 10^{-6} \text{ cm}^2/\text{s}$  to  $3.0 \times 10^{-5} \text{ cm}^2/\text{s}$  which is in much better agreement with the experimental measurement of  $2.2 \times 10^{-5} \text{ cm}^2/\text{s}$  for water in ambient conditions.

#### D. Recent Papers on Hybrid Functionals

More recent papers such as Ref.[53] argue that the most accurate XC functionals used in the simulation of water will need to include both a fraction of exact exchange and dispersion known as a hybrid functional. Previously, due to the relatively high computational cost, hybrid-based DFT was only performed on small gas phase clusters of water [54].

In Ref.[54], several GGA and hybrid functionals were used to compute and evaluate the energy and structure of H bonds of the four smallest  $\text{H}_2\text{O}$  clusters. The structure of these clusters are included in Fig.14 for illustrative purposes. For the clusters studied, it was concluded that the hybrid X3LYP [55] and PBE0 [56] functionals offered the best performance for H bonds in small water clusters when compared to GGAs. In particular, the BLYP [16][17] functional predicts H bonds that are too weak and the PBE [15] functional displayed variable performance depending on the cluster size.

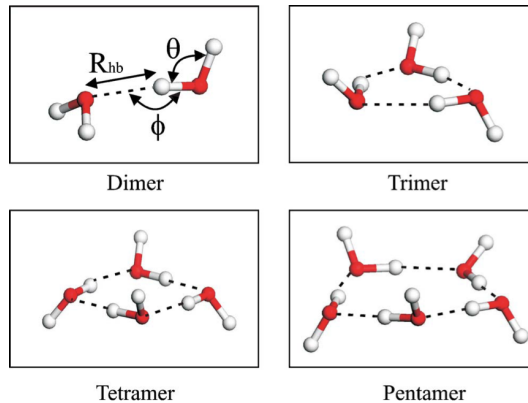


Fig. 14: The structure of the four water clusters examined where the dashed line indicate H bonds. Figure reproduced from Ref.[54].

### VII. Accounting for the Van Der Waals Forces

The “lack” of Van Der Waals forces, otherwise known as dispersion forces is one of the most significant problems of DFT. Because of this, DFT based forces which accurately accounts for dispersion have become a hot topic in computational physics, chemistry and material science. This is further highlighted in Fig.15.

The need for dispersion forces is due to the fact that standard XC functionals do not describe dispersion due to the following two reasons: instantaneous density fluctuations are not considered and only local properties are considered when calculating the XC energy. In this section, two systems which are incorrectly described by

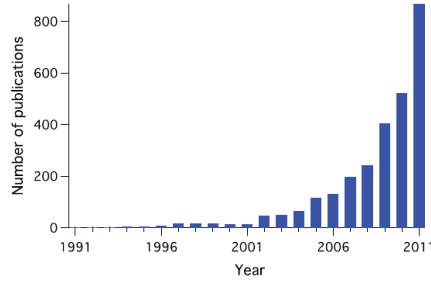


Fig. 15: The number of dispersion corrected DFT studies in recent years using Data from Web of Knowledge. Figure reproduced from Ref.[57]

the PBE functional will be highlighted. Current research involving corrections to the XC functionals to give a better description will then be reviewed.

### A. Examples of the limitation of XC functionals in systems involving dispersion

The lack of dispersion is particularly apparent in noble gases as the XC functionals describe binding or repulsion only when there is an overlap of the electron densities of the two atoms. As the overlap decays exponentially with interatomic separation, the binding also decays exponentially thus predicting incorrect properties. This is shown in Fig.16 using the PBE functional [15] for a binding curve between two Kr atoms. The dispersion originates from fluctuation in the electron density which polarize different atoms and molecules which can be seen on the right-hand side of the Fig.16. The interaction should exhibit the well known  $-1/r^6$  decay from the Van Der Waals force however the PBE functional gives an exponential decay for the interaction. This is because the PBE functional relies on the overlap of density to obtain the interaction.

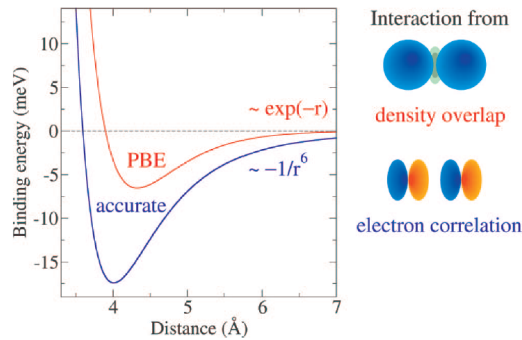


Fig. 16: The binding curves for Kr dimer which is obtained using the PBE XC functional and an accurate model potential [58]. Figure reproduced from Ref. [57].

A second more “real world” example demonstrating the limitations of the PBE functional is illustrated in Fig.17 involving a system of the DNA base pairs adenine and thymine in two different configurations. In the configuration on the left, the binding between the base pairs is dominated by Hydrogen bonding. As Hydrogen bonding is mainly governed by electrostatics, a standard functional such as the PBE will predict reasonable hydrogen bond strengths. Because of this, the stability is within 15% of the reference value [59]. On the other hand, the “stacked” configuration which can be seen on the right is dominated by dispersion forces and so the PBE functional is unable to predict the binding between the base pairs at all. This large discrepancy suggests that DNA simulated with PBE would not be stable.

### B. Common DFT based dispersion methods

This section will highlight some of the dispersion methods that are used to correct the XC functionals to give a more accurate description of dispersion forces. There is a vast amount of DFT based dispersion techniques that have been developed which for convenience can be grouped into methods which use similar approximations. In the order of increased accuracy at the cost of computational time, these groupings are: Binding with incorrect asymptotics, Simple C<sub>6</sub> corrections, Environment-dependent C<sub>6</sub> corrections, Long-range density functionals and

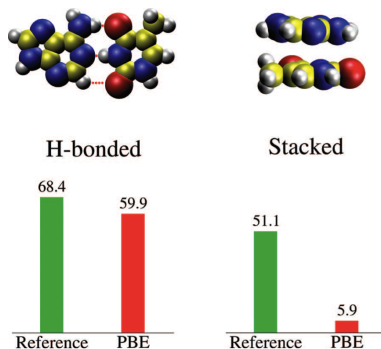


Fig. 17: Binding configurations of the DNA base pairs adenine and thymine. The hydrogen bonded structure with the hydrogen bonds indicated by red dots which can be seen on the left. The “stacked” configuration is on the right of the Figure. As can be seen, the Hydrogen bond configuration gives an accurate agreement with the reference data from Ref.[59]. In contrast, PBE fails to describe the binding of the “stacked” configuration where dispersion interactions are more significant. Figure reproduced from Ref.[57].

Beyond pairwise additivity. They are the topic of Ref.[57] and highlight one of the success stories in recent DFT research. A brief summary of some of these will be the topic of this subsection.

### B.1 Binding with incorrect asymptotics

Most XC functionals do not describe the long-range asymptotic energy and so they give an incorrect shape for the binding curves and underestimate the binding of well-separated molecules making them suitable to describe only weakly bonded systems. A solution to this is to use density functionals that are specifically fitted to reproduce weak interactions around the minima as well as using specific pseudopotentials. Minnesota functionals [60] are examples of functionals that are fitted to data sets that include properties such as the binding energies of dispersion bonded dimers. Despite being able to describe the binding accurately at separations around the minima, they have the same limitation in describing the energy at larger distances as LDA have. A solution for simulations that make use of pseudopotentials is to carefully fit potentials for each element however, this comes with effect that the pseudopotential is not easily transferable to other simulations.

### B.2 Simple $C_6$ corrections

A second solution to add  $-1/r^6$  asymptotic behaviour is to simply add an additional energy term that accounts for the the long-range attraction. Thus, the total energy will become

$$E_{\text{tot}} = E_{\text{DFT}} + E_{\text{disp}}, \quad (71)$$

where  $E_{\text{DFT}}$  is the total DFT energy computed with a given XC functional. The dispersion energy is given by

$$E_{\text{disp}} = - \sum_{A,B} \frac{C_6^{AB}}{r_{AB}^6}, \quad (72)$$

where the dispersion coefficients  $C_6^{AB}$  depend on the elemental pairs A and B and  $r_{AB}$  is the distance between the two elements. Despite this being a better approximation, there are still some shortcomings to it. One of these is that the  $C_6/r^6$  dependence represents only the leading term of the correction and neglects many-body dispersion effects from faster decaying terms such as the  $C_8/r^8$  and  $C_{10}/r^{10}$  interactions [61]. It is also unclear where the  $C_6$  coefficients should be obtained from and are typically fitted using experimental data which limits the number of elements the method can be used on. The  $C_6/r^6$  function also diverges for small  $r$  which is something that must be removed.

A more applicable method is known as the DFT-D2 correction in which the dispersion coefficients are calculated from a formula that couples ionization potentials and static polarizabilities of isolated atoms [62]. There is data for all elements up to Xe and the scheme was one of the most widely used methods to account for dispersion in DFT at the time. The paper compared a new B97-D functional that took into account the DFT-D2 correction along with other GGAs such as the BLYP and PBE functionals along with the B3LYP hybrid functional for standard thermochemical benchmark sets. It was concluded that the B97-D functional could be implemented in all efficient DFT programs. It was also likely to be the most accurate semi-empirical GGA available with the broadest range of applicability. It was also pointed out however that it still had the



self-interaction error which is a fundamental problem of all current GGAs. Thus, many reaction barriers will still be systematically underestimated when using the functional.

A more recent method known as DFT–D3 accounting for dispersion was published in Ref.[63]. In comparison to previous DFT–D variations such as DFT–D2 it had the following advantages and properties: It was less empirical as the most important parameters are computed from first principles using standard KS DFT. It also gives an almost exact dispersion energy for a gas of weakly interacting neutral atoms. It also provides a consistent description of elements with a nuclear charge of  $Z = 1$  to 94 as well as providing similar or better accuracy for “lighter” molecules as well as a strongly improved description of metallic and “heavier” systems. Ref.[63] also compared DFT–D3 with a variety of experimental results. Molecular  $C_6$  coefficients are experimentally known from dipole oscillator strength distributions (DOSDs) and thus a set of 174 pair coefficients for common molecules with a range of sizes were compared. The results can be seen graphically in Fig.18. It can be seen that method provides reliable coefficients of the entire range of the graph with a mean deviation of only 8.4%. Even for diatomic molecules such as  $N_2$  and  $O_2$  which typically have inaccurate descriptions as the atomic values are derived from very “different” molecules such as  $H_2O$  and  $NH_3$  the error is lower than 20%.

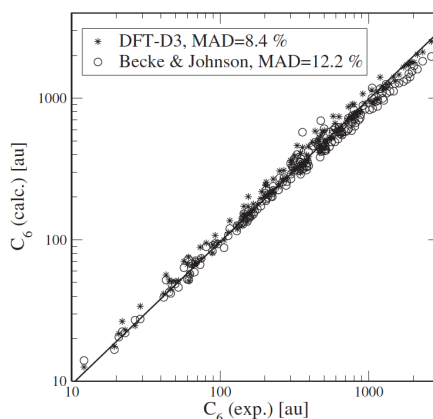


Fig. 18: Comparison of molecular  $C_6$  coefficients from DFT–D3 results with experimental DOSD values from Ref.[64]. The solid line has a slope of one and y intercept of zero. Figure reproduced from Ref.[63].

Overall, the paper concluded that the new DFT–D3 method can be used along with any standard density functional and can be applied to all elements on the Periodic Table as well as molecules and solid to achieve an accuracy within around 10% of experimental data. The DFT–D3 implementation also does not add significant computational cost compared to a typical GGA calculation so generally it is more accurate. However, it is also important to state that when applied to a particular problem, the accuracy should be verified against experimental data as in principle any approach can fail for a specific system.

## VIII. Summary and Conclusion

### A. Summary

To summarize, starting with the many-body Schrödinger equation, the KS equations were derived in Sec.II.. The approximations used to derive the equations were also highlighted so that the reader is made aware as to why CPMD may have some limitations when simulating certain properties such as the diffusion of water later discussed in Sec.VI.C.. Common methods used to solve the KS equations were then introduced in Sec.III. as these approximations are what make it possible to study complex systems involving many atoms. The procedure as to how the KS equations are solved using the methods was then summarized to give the reader an overview of how systems can be modelled.

The Car–Parrinello Lagrangian was then introduced in Sec.IV. along with the equations of motion that are what are solved using software packages to simulate systems. This gives a basic understanding of the physics behind CPMD such that applications of it are better understood. Why the Car–Parrinello method works is then discussed. These previous sections equip the reader with the fundamental tools to understand what can be researched in the field of DFT.

Sec.V. then gives a taster of the applications of DFT in medicine and material science. The section is rather qualitative; highlighting applications such as better understanding Prions which are a neurodegenerative disease and semiconductor photocatalysis which has potential application in the renewable energy sector.



The application of CPMD on the structure of water is then introduced in Sec.VI.. This section is very detailed due to the vast amount of literature available on the subject. Firstly, the different type of exchange and correction functionals first mentioned in Sec.II.H. were analyzed when applied to AIMD simulation of liquid water with their performance compared in Ref.[43]. It was found that the BLYP density functional yielded the best agreement with experiment. Ref.[47] concluded that temperature had a strong influence over the structure and dynamics of water. This was further emphasized in Sec.VI.C. when Ref.[51] highlighted that the diffusion coefficient of water,  $D$ , was out by a factor of 10 when compared to experiment. It was found that  $D$  would agree with experiment by increasing the temperature of classical simulations by 50K. Thus, the authors concluded that temperature had a large effect on the diffusion coefficient of water. Other reasons as to why simulations sometimes would not agree with experiments were also discussed. An important factor the authors mentioned was the accuracy of the exchange and correction functional used in the simulation. Alternative functionals are the topic of Sec.VI.D. and Sec.VII. where dispersion forces are considered.

Sec.VII.A. discusses why the lack of dispersion forces can give incorrect results for Hydrogen bonds for systems such as the DNA base pairs adenine and thymine. Corrections to XC functionals are then discussed in Sec.VII.B. and a recent method known as DFT-D3 using empirical data to give more accurate XC functionals is discussed.

## B. Conclusion

An important conclusion to draw from the review is that the earlier simulations of liquid water had less discrepancy to experimental data. As computational power increased so did the time scale and sample size of simulations. However, there was also an increase in discrepancy between different simulations and experiments. Ref.[47, 50, 51] all published in 2004 investigated these discrepancies found that it was an increase in the time scale and inaccurate XC functionals that had a contribution to the discrepancies. Thus, hybrid functionals and more accurate XC functionals are a hot topic in current DFT research.

Earlier simulations had a smaller timescale of around (10-20) ps which was restricted by computational power. The timescale can have a significant effect on the time interval of averages such radial distribution functions and strongly influence dynamical properties such as diffusion coefficients. It just so happened that at smaller time scales, the simulations had better agreement with experiment. It was also found that  $D$  would agree with experiment by increasing the temperature of classical simulations by 50K for certain systems in Ref.[51]. This indicates that there must be a quantum mechanical effect that needs to be considered that is more apparent at larger time scales and must have some dependence on temperature. This is likely the Van Der Waals force and is why it is such an important topic in current DFT research.

Despite some of these discrepancies, CPMD is an extremely successful field of research in a huge variety of disciplines and will likely grow. It is likely that in the future, it will be applied to even more complicated systems and will predict insightful properties. It is also important however for future research to understand the limitations of the method and more importantly what it is that causes them so that they can be overcome.

## References

- [1] P. Hohenberg and W. Kohn, “Inhomogeneous electron gas,” *Phys. Rev.*, vol. 136, pp. B864–B871, Nov 1964.
- [2] R. O. Jones, “Density functional theory: Its origins, rise to prominence, and future,” *Reviews of modern physics*, vol. 87, no. 3, p. 897, 2015.
- [3] R. Car and M. Parrinello, “Unified approach for molecular dynamics and density-functional theory,” *Physical review letters*, vol. 55, no. 22, p. 2471, 1985.
- [4] R. Car, “Introduction to density-functional theory and ab-initio molecular dynamics,” *Quantitative Structure-Activity Relationships*, vol. 21, no. 2, pp. 97–104, 2002.
- [5] J. Hutter, “Car parrinello molecular dynamics,” *Wiley Interdisciplinary Reviews: Computational Molecular Science*, vol. 2, no. 4, pp. 604–612, 2012.
- [6] S. S. Mallajosyula, J. C. Lin, D. L. Cox, S. K. Pati, and R. R. P. Singh, “Sequence dependent electron transport in wet dna: Ab initio and molecular dynamics studies,” *Phys. Rev. Lett.*, vol. 101, p. 176805, Oct 2008.
- [7] R. Car and M. Parrinello, “Structural, dynamical, and electronic properties of amorphous silicon: An ab initio molecular-dynamics study,” *Phys. Rev. Lett.*, vol. 60, pp. 204–207, Jan 1988.
- [8] F. Giustino, *Materials Modelling Using Density Functional Theory: Properties and Predictions*, pp. 19–22. Oxford University Press, 2014.
- [9] N. Bohr, “On the constitution of atoms and molecules,” *Philosophical Magazine*, vol. 26, no. 151, pp. 1–25, 1913.
- [10] J. C. Slater, “The theory of complex spectra,” *Phys. Rev.*, vol. 34, pp. 1293–1322, Nov 1929.
- [11] R. G. Parr, *Density-functional theory of atoms and molecules*. International series of monographs on chemistry ; 16, New York : Oxford University Press, 1994.
- [12] D. R. Hartree, “The wave mechanics of an atom with a non-coulomb central field. part i. theory and methods,” *Mathematical Proceedings of the Cambridge Philosophical Society*, vol. 24, no. 1, p. 89110, 1928.
- [13] V. Fock, “Näherungsmethode zur lösung des quantenmechanischen mehrkörperproblems,” *Zeitschrift für Physik*, vol. 61, no. 1, pp. 126–148, 1930.
- [14] W. Kohn and L. J. Sham, “Self-consistent equations including exchange and correlation effects,” *Phys. Rev.*, vol. 140, pp. A1133–A1138, Nov 1965.
- [15] J. P. Perdew, K. Burke, and M. Ernzerhof, “Generalized gradient approximation made simple,” *Phys. Rev. Lett.*, vol. 77, pp. 3865–3868, Oct 1996.
- [16] A. D. Becke, “Density functional exchange-energy approximation with correct asymptotic behavior,” *Phys. Rev. A*, vol. 38, pp. 3098–3100, Sep 1988.
- [17] C. Lee, W. Yang, and R. G. Parr, “Development of the colle-salvetti correlation-energy formula into a functional of the electron density,” *Phys. Rev. B*, vol. 37, pp. 785–789, Jan 1988.
- [18] A. D. Becke, “Density functional thermochemistry. ii. the effect of the perdewwang generalizedgradient correlation correction,” *The Journal of Chemical Physics*, vol. 97, no. 12, pp. 9173–9177, 1992.
- [19] J. P. Perdew, “Density functional approximation for the correlation energy of the inhomogeneous electron gas,” *Phys. Rev. B*, vol. 33, pp. 8822–8824, Jun 1986.
- [20] M. Sharma, R. Resta, and R. Car, “Intermolecular dynamical charge fluctuations in water: A signature of the h-bond network,” *Phys. Rev. Lett.*, vol. 95, p. 187401, Oct 2005.
- [21] C. Zhang, D. Donadio, F. Gygi, and G. Galli, “First principles simulations of the infrared spectrum of liquid water using hybrid density functionals,” *Journal of Chemical Theory and Computation*, p. 110321135603082, 03 2011.

- [22] M. Sharma, R. Resta, and R. Car, “Dipolar correlations and the dielectric permittivity of water,” *Phys. Rev. Lett.*, vol. 98, p. 247401, Jun 2007.
- [23] M. Krack, A. Gambirasio, and M. Parrinello, “Ab initio x-ray scattering of liquid water,” *The Journal of Chemical Physics*, vol. 117, no. 20, pp. 9409–9412, 2002.
- [24] S. M. Kathmann, I.-F. W. Kuo, C. J. Mundy, and G. K. Schenter, “Understanding the surface potential of water,” *The Journal of Physical Chemistry B*, vol. 115, no. 15, pp. 4369–4377, 2011. PMID: 21449605.
- [25] M. J. Gillan, D. Alfé, and A. Michaelides, “Perspective: How good is dft for water?,” *The Journal of Chemical Physics*, vol. 144, no. 13, p. 130901, 2016.
- [26] P. J. Hasnip, K. Refson, M. I. J. Probert, J. R. Yates, S. J. Clark, and C. J. Pickard, “Density functional theory in the solid state,” *Philosophical transactions. Series A, Mathematical, physical, and engineering sciences*, vol. 372, March 2014.
- [27] D. Marx and J. Hutter, *Ab initio molecular dynamics : basic theory and advanced methods*. Cambridge: Cambridge University Press, 2012.
- [28] G. Pastore, E. Smargiassi, and F. Buda, “Theory of ab initio molecular-dynamics calculations,” *Physical Review A*, vol. 44, no. 10, p. 6334, 1991.
- [29] N. N. Bogoliubov, Y. A. Mitropolsky, and J. Gillis, *Asymptotic Methods in the Theory of Non-Linear Oscillations*, vol. 16. Hindustan Publishing Corporation, 01 1963.
- [30] H. Tong, S. Ouyang, Y. Bi, N. Umezawa, M. Oshikiri, and J. Ye, “Nano-photocatalytic materials: Possibilities and challenges,” *Advanced Materials*, vol. 24, no. 2, pp. 229–251, 2012.
- [31] Z. G. Zou, T. Shishido, J. H. Ye, and M. Oshikiri, “New visible light driven semiconductor photocatalysts and their applications as functional eco-materials,” in *Functionally Graded Materials VII*, vol. 423 of *Materials Science Forum*, pp. 825–0, Trans Tech Publications, 3 2003.
- [32] M. Oshikiri, M. Boero, A. Matsushita, and J. Ye, “Water adsorption onto y and v sites at the surface of the yvo4 photocatalyst and related electronic properties,” *The Journal of Chemical Physics*, vol. 131, no. 3, p. 034701, 2009.
- [33] E. Mosconi, J. M. Azpiroz, and F. De Angelis, “Ab initio molecular dynamics simulations of methylammonium lead iodide perovskite degradation by water,” *Chemistry of Materials*, vol. 27, no. 13, pp. 4885–4892, 2015.
- [34] P. Carloni, U. Rothlisberger, and M. Parrinello, “The role and perspective of ab initio molecular dynamics in the study of biological systems,” *Accounts of Chemical Research*, vol. 35, no. 6, pp. 455–464, 2002. PMID: 12069631.
- [35] A. L. Horwich and J. S. Weissman, “Deadly conformations—protein misfolding in prion disease,” *Cell*, vol. 89, May 1997.
- [36] S. Van Doorslaer, G. M. Cereghetti, R. Glockshuber, and A. Schweiger, “Unraveling the cu<sup>2+</sup> binding sites in the c-terminal domain of the murine prion protein: a pulse epr and endor study,” *The Journal of Physical Chemistry B*, vol. 105, no. 8, pp. 1631–1639, 2001.
- [37] P. Zatta, D. Drago, S. Bolognin, and S. L. Sensi, “Alzheimer’s disease, metal ions and metal homeostatic therapy,” *Trends in Pharmacological Sciences*, vol. 30, no. 7, pp. 346 – 355, 2009.
- [38] A. Gaeta and R. C. Hider, “The crucial role of metal ions in neurodegeneration: the basis for a promising therapeutic strategy,” *British Journal of Pharmacology*, vol. 146, pp. 1041–1059, December 2005.
- [39] M. C. Colombo, L. Guidoni, A. Laio, A. Magistrato, P. Maurer, S. Piana, U. Rohrig, K. Spiegel, M. Sulpizi, J. VandeVondele, M. Zumstein, and U. Rothlisberger, “Hybrid QM/MM Car-Parrinello simulations of catalytic and enzymatic reactions,” *Chimia*, vol. 56, no. 1-2, pp. 13–19, 2002.
- [40] S. Piana and P. Carloni, “Conformational flexibility of the catalytic asp dyad in hiv-1 protease: An ab initio study on the free enzyme,” *Proteins: Structure, Function, and Bioinformatics*, vol. 39, no. 1, pp. 26–36, 2000.

- [41] K. Laasonen, M. Sprik, M. Parrinello, and R. Car, “ab initio liquid water,” *The Journal of Chemical Physics*, vol. 99, no. 11, pp. 9080–9089, 1993.
- [42] A. Soper and M. Phillips, “A new determination of the structure of water at 25c. chem. phys.107, 47-60,” *The Journal of Chemical Physics*, vol. 107, pp. 47–60, 08 1986.
- [43] M. Sprik, J. Hutter, and M. Parrinello, “Ab initio molecular dynamics simulation of liquid water: Comparison of three gradient corrected density functionals,” *The Journal of Chemical Physics*, vol. 105, no. 3, pp. 1142–1152, 1996.
- [44] P. L. Silvestrelli and M. Parrinello, “Structural, electronic, and bonding properties of liquid water from first principles,” *The Journal of Chemical Physics*, vol. 111, no. 8, pp. 3572–3580, 1999.
- [45] A. Botti, F. Bruni, M. A. Ricci, and A. K. Soper, “Neutron diffraction study of high density supercritical water,” *The Journal of Chemical Physics*, vol. 109, no. 8, pp. 3180–3184, 1998.
- [46] A. H. Narten and H. A. Levy, “Liquid water: Molecular correlation functions from xray diffraction,” *The Journal of Chemical Physics*, vol. 55, no. 5, pp. 2263–2269, 1971.
- [47] J. VandeVondele, F. Mohamed, M. Krack, J. Hutter, M. Sprik, and M. Parrinello, “The influence of temperature and density functional models in ab initio molecular dynamics simulation of liquid water,” *The Journal of Chemical Physics*, vol. 122, no. 1, p. 014515, 2005.
- [48] J. C. Grossman, E. Schwegler, E. W. Draeger, F. Gygi, and G. Galli, “Towards an assessment of the accuracy of density functional theory for first principles simulations of water,” *The Journal of Chemical Physics*, vol. 120, no. 1, pp. 300–311, 2004.
- [49] D. Prendergast, J. C. Grossman, and G. Galli, “The electronic structure of liquid water within density-functional theory,” *The Journal of Chemical Physics*, vol. 123, no. 1, p. 014501, 2005.
- [50] J. C. Grossman, E. Schwegler, E. W. Draeger, F. Gygi, and G. Galli, “Towards an assessment of the accuracy of density functional theory for first principles simulations of water,” *The Journal of Chemical Physics*, vol. 120, no. 1, pp. 300–311, 2004.
- [51] E. Schwegler, J. C. Grossman, F. Gygi, and G. Galli, “Towards an assessment of the accuracy of density functional theory for first principles simulations of water. ii,” *The Journal of Chemical Physics*, vol. 121, no. 11, pp. 5400–5409, 2004.
- [52] R. Mills, “Self-diffusion in normal and heavy water in the range 1-45.deg.,” *The Journal of Physical Chemistry*, vol. 77, no. 5, pp. 685–688, 1973.
- [53] R. A. D. Jr., B. Santra, Z. Li, X. Wu, and R. Car, “The individual and collective effects of exact exchange and dispersion interactions on the ab initio structure of liquid water,” *The Journal of Chemical Physics*, vol. 141, no. 8, p. 084502, 2014.
- [54] B. Santra, A. Michaelides, and M. Scheffler, “On the accuracy of density functional theory exchange-correlation functionals for h bonds in small water clusters: Benchmarks approaching the complete basis set limit,” *The Journal of Chemical Physics*, vol. 127, no. 18, p. 184104, 2007.
- [55] X. Xu and W. A. Goddard, “The x3lyp extended density functional for accurate descriptions of nonbond interactions, spin states, and thermochemical properties,” *Proceedings of the National Academy of Sciences of the United States of America*, vol. 101, no. 9, pp. 2673–2677, 2004.
- [56] C. Adamo and V. Barone, “Toward reliable density functional methods without adjustable parameters: The pbe0 model,” *The Journal of Chemical Physics*, vol. 110, no. 13, pp. 6158–6170, 1999.
- [57] J. Klime and A. Michaelides, “Perspective: Advances and challenges in treating van der waals dispersion forces in density functional theory,” *The Journal of Chemical Physics*, vol. 137, no. 12, p. 120901, 2012.
- [58] K. T. Tang and J. P. Toennies, “The van der waals potentials between all the rare gas atoms from he to rn,” *The Journal of Chemical Physics*, vol. 118, no. 11, pp. 4976–4983, 2003.
- [59] P. Jurecka, J. Sponer, J. Cerny, and P. Hobza, “Benchmark database of accurate (mp2 and ccSD(T) complete basis set limit) interaction energies of small model complexes, dna base pairs, and amino acid pairs,” *Phys. Chem. Chem. Phys.*, vol. 8, pp. 1985–1993, 2006.

- [60] H. Krieg and S. Grimme, “Thermochemical benchmarking of hydrocarbon bond separation reaction energies: Jacob’s ladder is not reversed!,” *Molecular Physics*, vol. 108, no. 19-20, pp. 2655–2666, 2010.
- [61] J. F. Dobson, A. White, and A. Rubio, “Asymptotics of the dispersion interaction: Analytic benchmarks for van der waals energy functionals,” *Phys. Rev. Lett.*, vol. 96, p. 073201, Feb 2006.
- [62] S. Grimme, “Semiempirical ggatype density functional constructed with a longrange dispersion correction,” *Journal of Computational Chemistry*, vol. 27, pp. 1787–1799, November 2006.
- [63] S. Grimme, J. Antony, S. Ehrlich, and H. Krieg, “A consistent and accurate ab initio parametrization of density functional dispersion correction (dft-d) for the 94 elements h-pu,” *The Journal of Chemical Physics*, vol. 132, no. 15, p. 154104, 2010.
- [64] E. R. Johnson and A. D. Becke, “A post-hartree–fock model of intermolecular interactions,” *The Journal of Chemical Physics*, vol. 123, no. 2, p. 024101, 2005.